Artificial source techniques : brief survey

Typically used to explore crust at shallow depths. The method in most common use today is seismic reflection profiling. Used by oil companies in exploring for oil-bearing formations, both at sea and on land.

Also employed for strictly scientific purposes, e.g. in exploring ocean crust, depth of sediments, etc.

Sea: common to use airgun or sparker source, e.g. used continuously by Glomar Challenger in steaming between DSDP sites or in surveying sites

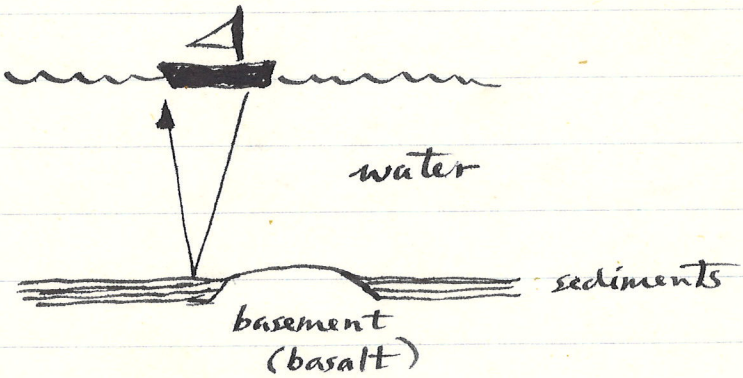

Seismic waves are reflected off horizons where ∃ discontinuities in properties.

DGE NORFOLK BASIN

THREE KINGS
RISE

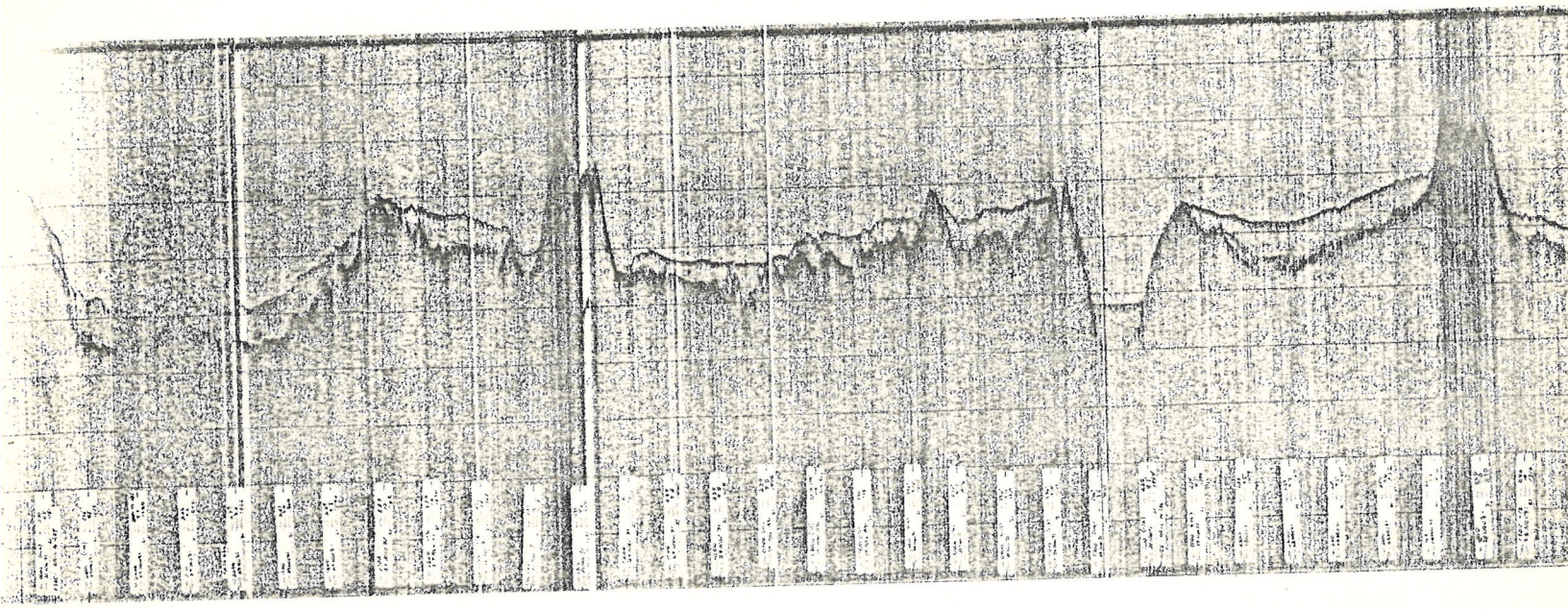

DAMPIER

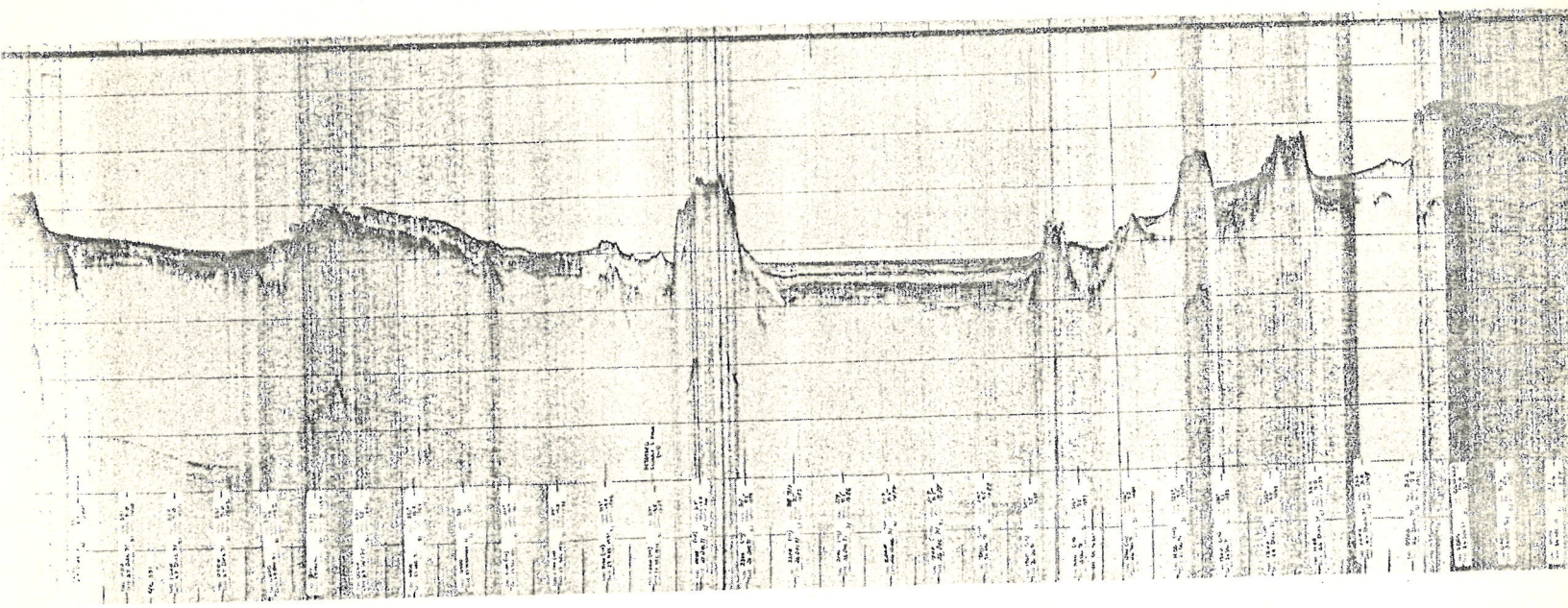

Typically one just lines up the traces. The vertical coordinate is 2-way travel time of the wave in seconds, but apart from that the display has the flavor of a geological cross-section. Penetration is typically a few kilometers into crust. Multiples or ghosts arise from reflections off upper surface of ocean. These are occasionally troublesome.

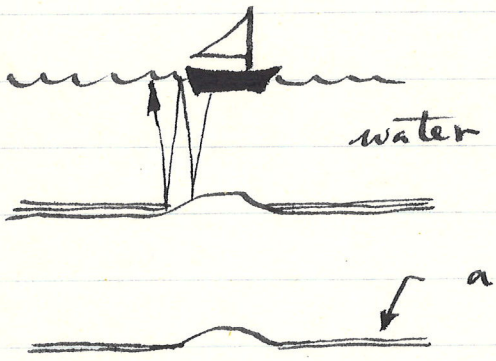

Land: one uses dynamite in holes or more modern technique which can even be used in populated areas Vibroseis®, a large truck which can be raised up on a foot and shaken. Procedure here typically uses long arrays of geophones as receivers and the data are CDP stacked for the final output.

3B.3 PRACTICAL METHODS OF INTRODUCING THE INPUT SIGNAL INTO THE EARTH—VIBRATOR DESIGN PRINCIPLES

Having selected the signal needed, there remains the problem of introducing such a primary signal into the ground. The conventional method (see Crawford, Doty, and Lee, 1960) has been to vibrate a large plate (called the baseplate) which is kept in contact with the ground during the time of generation of the signal. If the vibratory signal desired has a range of force of $2A$ pounds, the baseplate must be held down on the ground with a force of at least A pounds, since otherwise it would leave the ground and hammering would result. The weight of the vehicle is used as the hold-down weight, and the vehicle is isolated from the vibration by air bags or similar "soft" springs. With the weight of the truck on it, the system corresponds to a very low-frequency-damped resonant system. The period is kept well below the lowest frequency to be generated by the vibrator. Large, heavy vehicles are therefore necessary to have a high enough mass to hold down the vibrator, as well as to carry the weight of the diesel power supplies, vibrator units, and auxiliary equipment. With the continual demand for increasing the low-frequency characteristics of vibrators, a compromise is becoming necessary between the weight of vehicles, their maneuverability, and road weight limits.

The vibrator mechanism is attached to the lift system through the isolating air bags, and it can be raised or lowered onto the ground by hydraulic cylinders capable of lifting the entire truck off the ground so that its weight is fully on the baseplate.

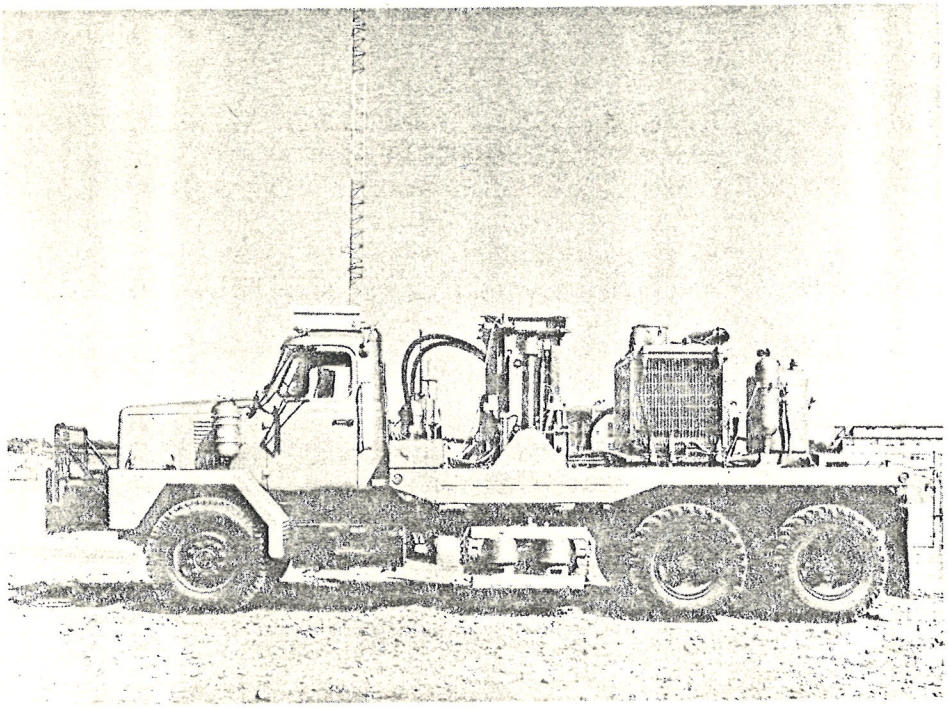

Plate 1 A standard Conoco Model 8 vertical vibrator. Peak force 19,000 lb; low-frequency limit 4.7 Hz.

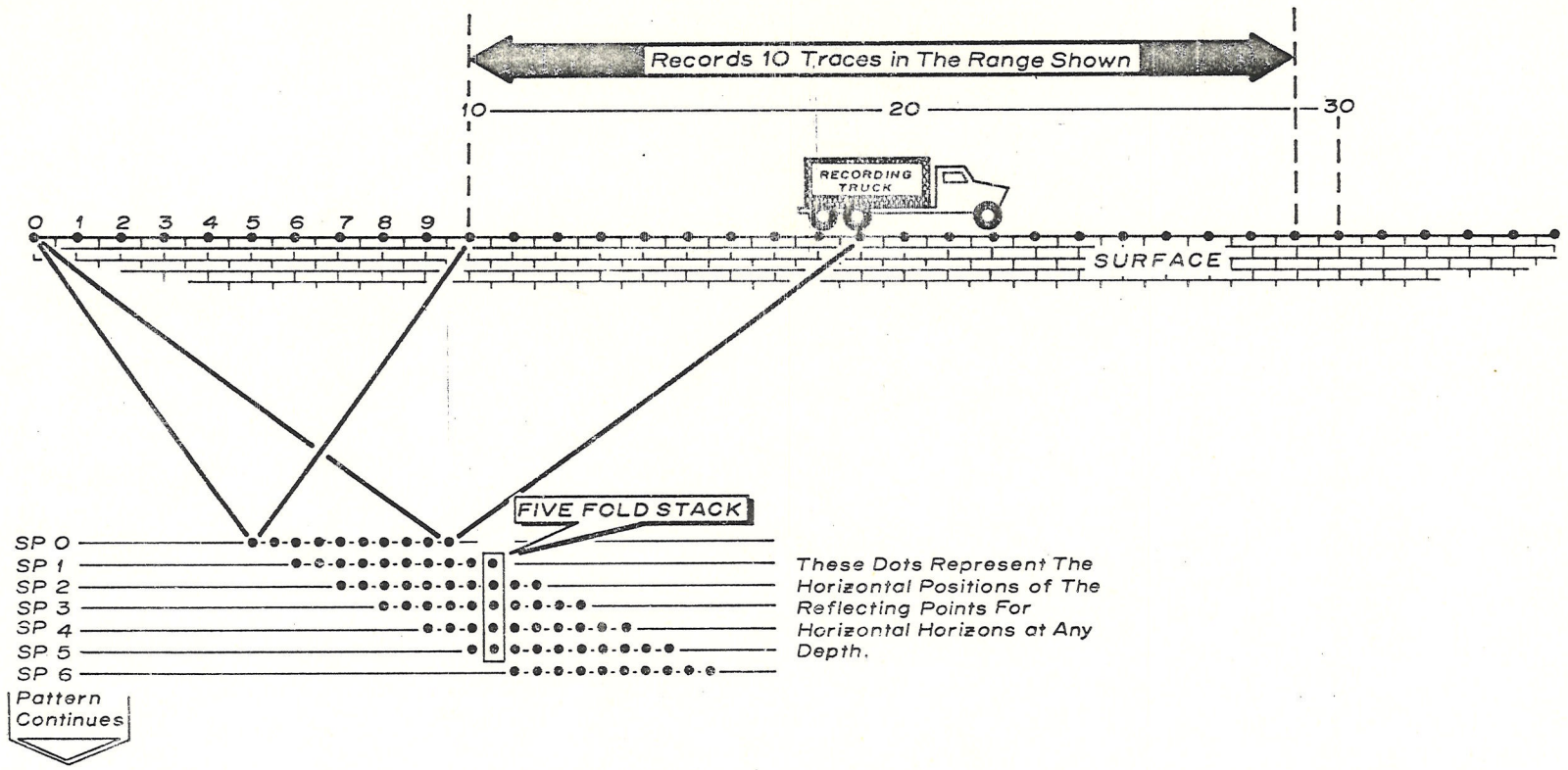

Figure 5.5 The basic arrangement of a typical (fivefold) CDP reflection spread. The recording truck contains a switch which allows selection of the correct sequence of geophones as the shot point is moved up. As convenient, portions of cable and geophones are moved from the left end and connected to the right end of the cable.

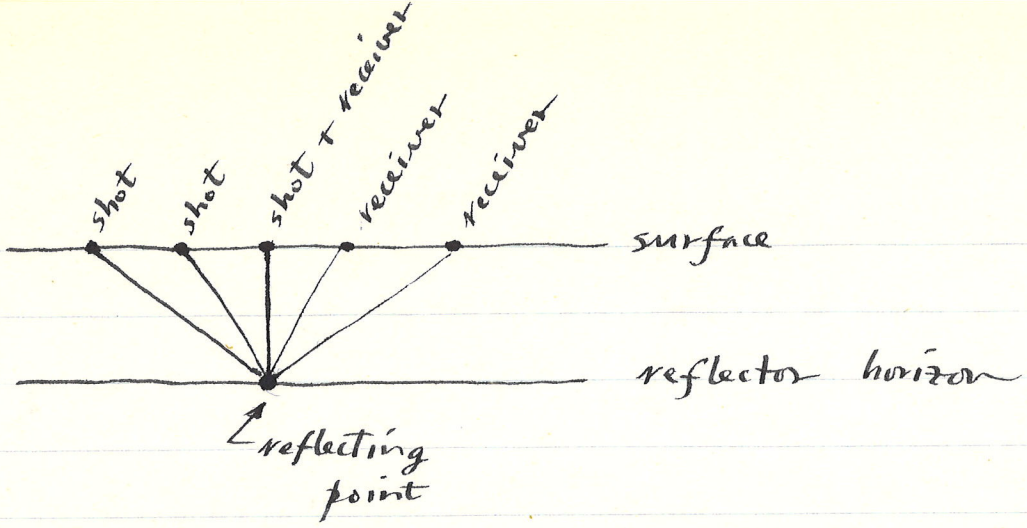

Simple delay and sum stacking puts all energy from same point reflector in the same place. Reflection seismology a very specialized subject, the sole occupation of ~1/2 the world's seismologists.

Recent project to use same techniques in non-likely-oil-prospect areas to investigate tectonic problems, other strictly scientific questions, COCORP. An example of power of this technique Wind River Mtn profile in Wyoming

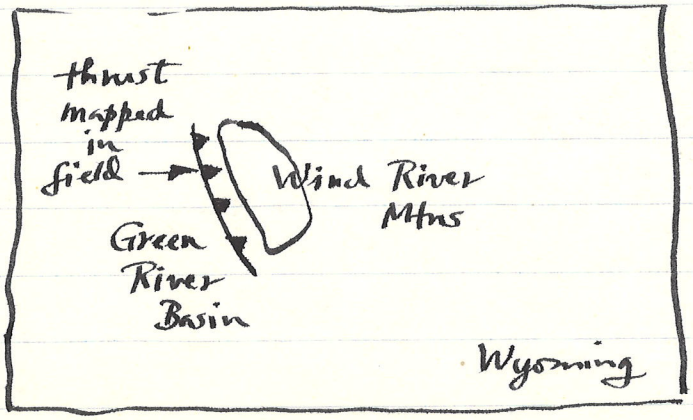

Question: what is the attitude of the thrust at depth? Two postulated scenarios

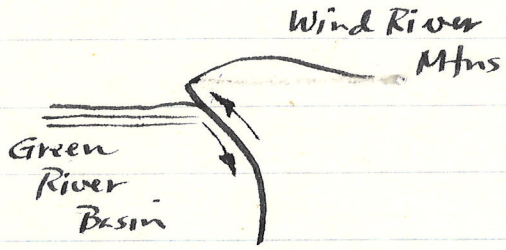

fault steepens, this a block uplift model, no compression or crustal shortening required

fault continues at same dip or gets shallower, this is thrust uplift due to compression, associated with plate tectonics

The COCORP profile shows the thrust continuing down to at least 8 s two-way travel time, corresponds to ~ 30 km, in agreement with the second model.

The second technique is the seismic refraction method, does not have the spatial resolution of seismic reflection

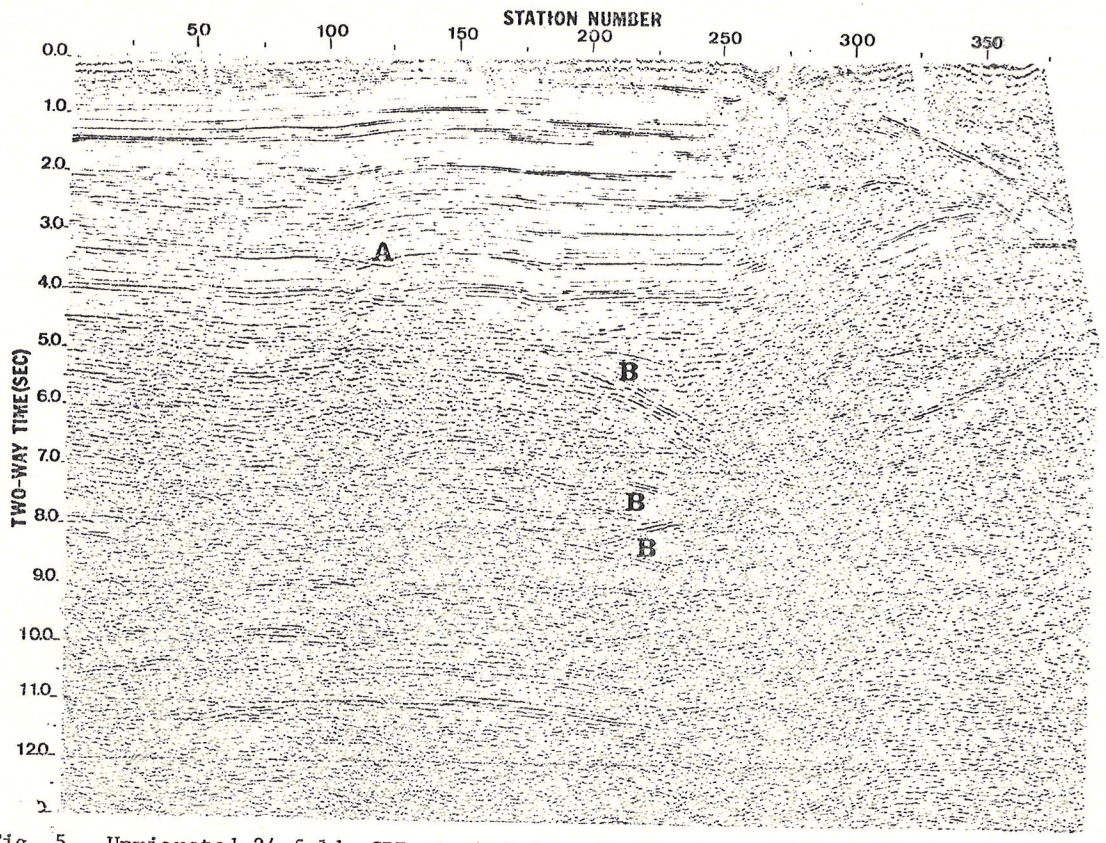

Fig. 5. Unmigrated 24-fold, CDP-stacked Cocorp reflection profile showing line 1. Station numbers along top. Flat lying sedimentary rocks of Green River Basin from surface down to 4.0-4.5 s. Excellent data quality ends at station 250, where the Wind River thrust approaches the surface, bringing a wedge of Precambrian crystalline rocks above sedimentary rocks. Pacific Creek anticline is clearly visible in the sedimentary rocks at station 150. A syncline on the west side of the anticline gives the characteristic bow tie effect of a syncline with a buried focus (A). Highly dipping events (B, 5-9 s) may be reflections from outside the plane of the section (sideswipe). Strong reflections continue down to 11 s.

higher peak frequency (about 12-15 Hz versus 20-25 Hz) at 9-10 s in lines 1 and 1A, where Precambrian is exposed so that higher frequencies are usable in crystalline rocks.

Signal-to-noise ratio is variable probably because of wind on certain days, especially later in the fall on bases of coherence and noncoherent energy. A signal-to-noise ratio of 1 is reached at about 15 s on line 1, 13 s on line 1A, and 10 s on line 2. The data is presented unmigrated in time sections so that true position and geometry of structures are distorted. Readers should note that seismic time sections do not show the true position or even the true geometry of reflectors and that interpretation may be complicated by events arriving obliquely from outside the plane of the section.

Anomalous Events

Anomalous events on the seismic sections include multiple reflections, reflected refractions, diffractions, energy from events arriving outside the plane of the section, and possibly converted waves. Of these, multiple reflections are the most common and constitute a significant part of the events in parts of lines 1 and 2.

Recognition of multiple reflections on a broad scale is based on two criteria: (1) general parallelism of deep reflections with surface structure in sedimentary rocks (Figures 5 and 7) and (2) the total change character of seismic sections between lines 1 and 2 (Figures 5 and 7), where sedimentary rocks cover the surface, and line 1A (Figure 6), where Precambrian rocks crop out. In lines 1 and 2, reflections as deep as 10-12 s mirror the dip of sedimentary rocks in the first 2-4 s. The resulting broad pattern is that numerous closely spaced horizontal reflectors are found between 4 and 12 s on the left-hand side of line 1 (Figure 8). Here the basement is at 4.5 s or less. The nature of the multiple problem is clearly illustrated by observing a typical 'bow tie' pattern from a syncline with a buried focus (Figure 9). This pattern occurs at 3.5 and 4.0 s as primary reflections and is repeated as multiple reflections at 6-7 s, a time far below the base of the Cambrian in this area. These multiple reflections appear best on the near-trace stack (Figure 9) where the normal-moveout of the multiples is too small for them to be cancelled. Multiples repeated at 400-600 ms suggest that events are being repeated by a relatively short path which may be in the near surface. Similarity in character between horizontal events from 5 to 12 s

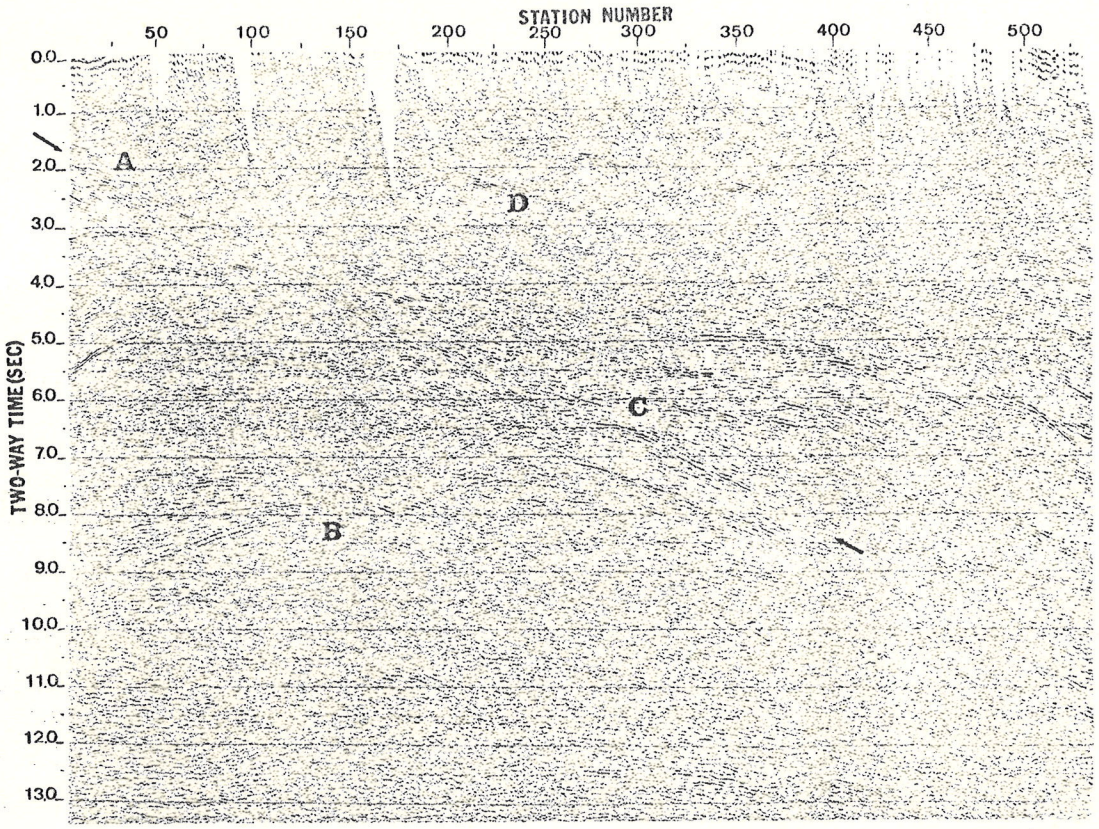

Fig. 6. Cocorp reflection profile showing line 1A. Wind River thrust (arrows) is a continuous reflection to 9.0 s or 24 km. Strong reflection (A, upper left) marks wedge of Precambrian crystalline rocks overlying sedimentary rocks to 3.9 s. Velocity uplift, complex faulting, and possibly folding in sedimentary rocks under the thrust. Precambrian rocks exposed at the surface from stations 100 to 175 of line 1A. Complex Precambrian structure in the deep crust (B at 8 s, C at 6 s) may be correlated across the fault. Strong shallow reflection (D) in Precambrian crust.

and those in the sedimentary section is striking (Figures 8 and 9). Likewise, the dipping events on the left side of line 2 (Figure 7) strongly mirror structure in sedimentary rocks and probably are multiple reflections. A dead zone for about 2 s beneath the sedimentary reflections here probably represents the time interval in which the CDP filter is successfully cancelling multiples and in which trace amplitude is decreased by automatic gain control. In sharp contrast is the general appearance or character of reflections in the middle part of line 1A (Figure 6). Here the reflections are much less common and weaker and show divergent dips and less regular character, exactly what would be expected from complex basement rocks. Theory tells us that any multiple reflections should decrease rapidly in amplitude. The strength of these multiple reflections is probably caused by constructive interference within the multiple-generating system. Certainly, this area, which has been well prospected, is not known to be a problem area for multiples caused by certain high-amplitude reflectors [Ellsworth, 1948; Mouritsen, 1963] that interfere within the sedimentary reflections. Reflection coefficients for single interfaces are up to 0.3 in sedimentary rocks and 0.13 in crystalline rocks. When we consider the capability for much stronger reflections in the sedimentary section, sedimentary multiples may overwhelm primary reflections from within underlying basement, whereas such multiples would simply go unnoticed within record times for sedimentary rocks.

Reflected refractions seem to be a common kind of noise associated with faulted anticlines in Laramide structures. These events are typically caused by a refraction from a high-speed layer hitting a reflector such as a fault and reversing their path along the high-speed layer to return to the surface as a head wave. They appear as crosscutting events with high constant dips [Swartz and Lindsey, 1942]. Good examples are found in the middle of line 2 (Figure 7), where an event dipping steeply to the left comes off the Sand Draw anticline. It has an apparent velocity of 5.9 km/s and probably corresponds to a refraction that was reflected from the reverse fault in the Sand Draw anticline along the top of a sedimentary layer. A similar event at 5 s beneath the Wind River thrust (Figure 10) has an apparent velocity of 7.0 km/s and may be a primary event representing important structure such as a crustal flake [Oxburgh, 1972] related to the fault, or it may be a reflected refraction or other anomalous event such as a reflection that traveled a complex path underneath the Precambrian fault wedge.

Energy from a reflector lying outside the plane of the section (sideswipe) [Tucker and

Can be done either on land or at sea. Source almost always an explosive since need to receive signal at fairly large distances.

Example: say a 3 layer medium

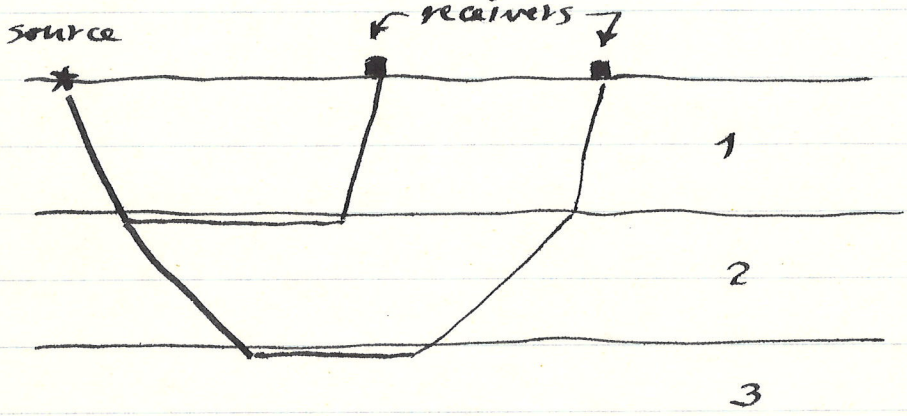

Old technique measured only arrival time of first arriving signal. At distances $\geq$ depth this will be the head wave or refracted wave. If structure of crust is really 3-layered as shown then plot of T vs. distance will consist of 3 line segments

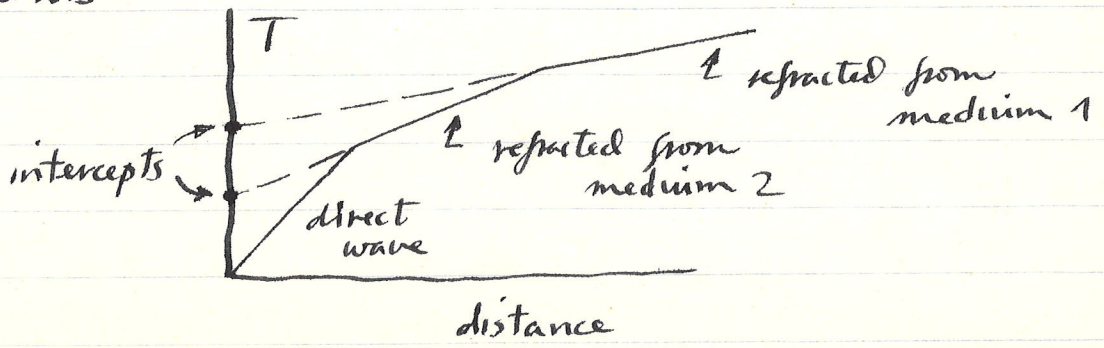

Beneath normal ocean basins, the Moho is about 11 km below sea-level and the oceanic crust is about 6–7 km thick. Layer 1 which consists of sediments is locally absent on the flanks and crests of ridges and at the other extreme it reaches over 3 km in parts of the Argentine basin (EWING, 1965). As the velocity within layer 1 increases with depth (see below), the thickness estimates based solely on refraction data must somewhat underestimate the true thickness. Layer 2 is the most variable in thickness and velocity, although accurate estimates of its velocity are difficult to obtain. In the normal parts of the Pacific it averages 1·3 km but it is about 2·4 km thick beneath archipelagic aprons (MENARD, 1964). Layer 3, which is the main oceanic crustal layer, is the most uniform in thickness and velocity.

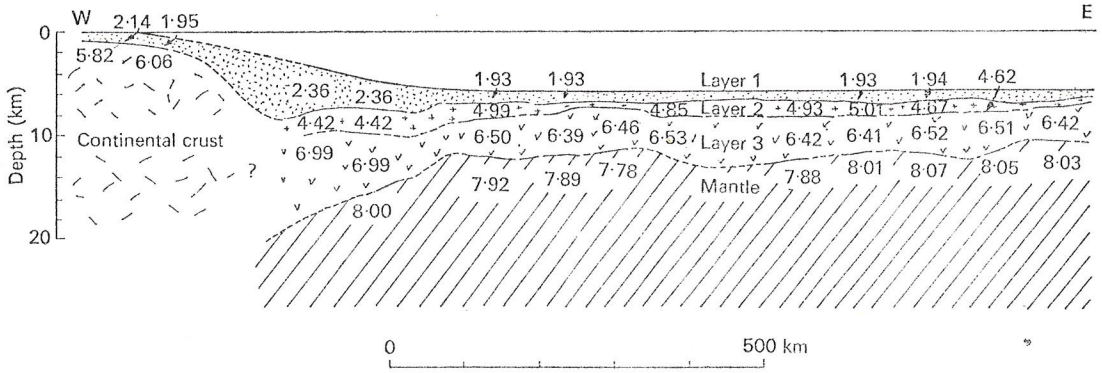

Fig. 3.3 Oceanic crustal structure as determined by refraction lines in the Atlantic Ocean east of Argentine. The line runs from (46·0° S, 60·3 °W) on the shelf to (42·7° S, 50·2 °W) in the ocean. Redrawn from EWING (1965), *Q. Jl. R. astr. Soc.*, **6**, 19.

An example of the results of refraction surveys is shown in Figure 3.3. This is a profile over part of the Argentine basin.

Seismic reflection profiling

A much more detailed picture of the structure within layer 1 and of the shape of the layer 1/layer 2 interface is obtained by seismic reflection profiling as described by EWING and ZAUNERE (1964). The method is akin to echo-sounding except that the sound source is more powerful and has a lower frequency content, enabling the waves to penetrate below the ocean-floor and to be reflected from interfaces below before attenuation has reduced the amplitude below the detection limit. The early method was to set off small explosive charges at regular time intervals while the ship was under way, but nowadays other types of acoustic sources such as air-guns are mainly used. The return waves are received by a towed hydrophone array and are recorded visually or on magnetic tape. A record is shown in Figure 3.4.

The reflection records yield the two-way travel-time to the reflecting horizons. This can only be converted to depth if the velocity distribution below the seabed is assumed or determined by other methods (see below). The prominence of a given reflection on the record depends on the amplitude of the reflected wave. The relative amplitudes of reflected and incident waves at an interface is called the reflection coefficient r, and it is given by

$$r = (\rho_1 V_1 - \rho_2 V_2)/(\rho_1 V_1 + \rho_2 V_2)$$

where ρ_i and V_i are the densities and P velocities of the rocks above and below the interface. A large contrast in ρV at an interface means a strong reflection.

Then slope of line $dx/dt = 1/\alpha$ of layer and intercept depends on layer thickness. Can thus find both. One actually measures an average of the structure between source and receivers, typically 50 – 100 km in oceanic refraction surveys.

Modern approach makes use of entire recorded signal, compare with synthetic seismograms generated on computers. Model of velocity structure of oceanic crust now fairly well established. See figure 3 of Spudich + Orcutt. Moho at 8 – 10 km depth typically, α goes from 6 – 7 km/s to about 8 km/s.

Synthetics include secondary arrivals, wide angle reflections, etc.

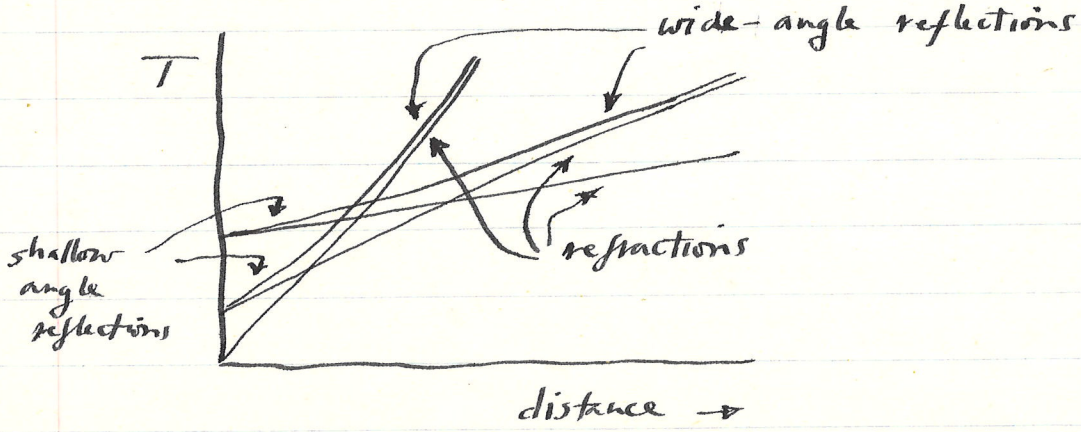

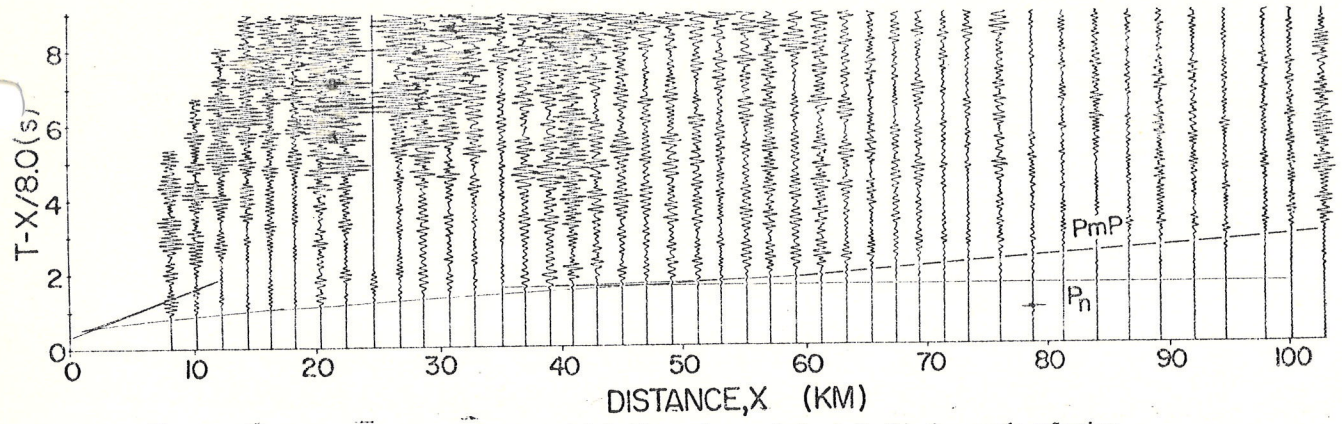

Fig. 4. Data from which the models in Figure 3 were derived. *PmP* is the mantle reflection.

layer 3 and mantle velocities. However, they differ substantially regarding the nature of layer 2 and the crust-mantle transition. A similar situation can be seen in Figure 3, which shows three velocity-depth profiles presented by *Orcutt et al.* [1977] which satisfy the first-arrival time data from a refraction profile that they shot using ocean bottom seismometers. Note that one of the velocity-depth profiles has a sharp crust-mantle discontinuity, while another has practically no mantle transition zone whatever. The same is true of the two velocity profiles presented for DW34 in Figure 2. If one wished to learn about the thickness or existence of the Moho at these sites, one could say nothing about it on the basis of the first-arrival travel time data, which are usually regarded as the primary data in a refraction experiment.

To choose from among these velocity models, one must use some of the additional information available in the seismograms. For example, a clear difference between the two different velocity models for DW34 is that the layered model predicts the existence of reflections from the top of layer 3 and the mantle, labeled according to the nomenclature system proposed by *Spudich and Orcutt* [1980] as *P3P* and *PmP* in Figure 1. Similarly, from two of the three velocity profiles in Figure 3 we would expect to see some sort of mantle reflection in the seismograms, and from the third profile we expect none. Examination of the data themselves in Figure 4 reveals a conspicuous mantle reflection, *PmP*. Thus we can immediately rule out the velocity model with no Moho, although it is still not clear without quantitative analysis which of the remaining two profiles is more correct.

The above examples show that considerably more information about the earth's velocity structure can be extracted from seismograms if we use the existence and amplitudes of seismic phases as well as first-arrival times as data. It is the consideration of these additional data which has helped change our view of the oceanic crust. In the above example we used a qualitative argument about the size of *PmP* to learn about the Moho transition at a particular site (as does *Prodehl* [1977] for European and North American sites), but this can also be done in a more quantitative way by using recently developed theoretical and computational techniques to model observed seismograms' arrival times, amplitudes, and waveforms.

This approach to analyzing real seismograms was pioneered by *Helmberger* [1968], *Helmberger and Morris* [1969, 1970], and *Fuchs and Müller* [1971]. The methods that they developed allow them to test the reality of hypothetical earth models, consisting of *P* and *S* wave velocity-depth profiles and a density-depth profile, by first specifying the locations of a seismic source and receiver at or near the surface of their earth model and then computing the seismograms which would be observed at the receiver because of the propagation of seismic waves through their hypothetical earth model from the source. Using this approach, one could propose a hypothetical velocity and density model of the oceanic crust and upper mantle, for example, and compute the seismogram which would be observed at 20-km range from a 5-kg shot. Comparison of these synthetic seismograms with observed seismograms provides a powerful means for testing hypothetical earth models, since this method enables one to insist that both the seismic wave travel times and the amplitudes predicted by a trial earth model agree with observations.

To show the utility of this method, we can test the often cited 'average oceanic crust' model which *Raitt* [1963] obtained by averaging together all the layered crustal models available at that time from deep ocean refraction stations. The specific velocity model that we have used consists of Raitt's average *P* velocities in layers 2 and 3 and the mantle, overlain by 170 m of unconsolidated sediment and a uniform 5-km-deep ocean, as shown in Figure 5. Crustal shear velocities have been obtained by assuming a Poisson's ratio of 0.25. As seismic sources we have used the pressure functions appropriate to explosive charges of 1- to 45-kg weight detonated at typical depths (quarter-wave depth, ~50 m) beneath the wa-

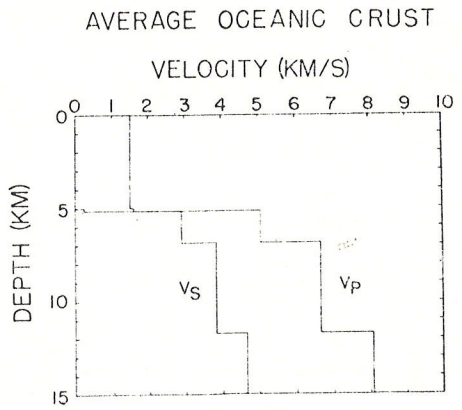

Fig. 5. Average oceanic crust model. The top two layers are water and unconsolidated sediment. *P* velocities and layer thicknesses are taken from *Raitt* [1963]. Crustal *S* velocities are derived from the assumption of a 0.25 value of crustal Poisson's ratio.

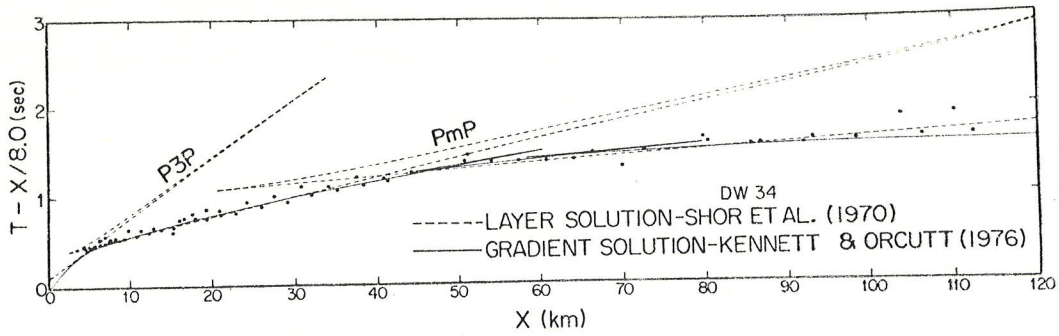

Fig. 1. DW34 first-arrival travel time data and travel time curves from the two velocity models in Figure 2. *P3P* and *PmP* are reflections off the tops of layer 3 and the mantle in the layer solution model in Figure 2.

mogeneous layers bounded by horizontal or dipping planes, derived from the assumption that the compressional or shear wave arrivals observed in a seismic experiment have been critically refracted as head waves or conical waves along the tops of various layers. The layered structures derived from explosion seismology, such as those of *Shor et al.* [1970], fall into this category, as do the basal layers of *Maynard* [1970] and *Sutton et al.* [1971] and the layers 2A, 2B, and 2C of *Houtz and Ewing* [1976]. We shall refer to such layered models as 'layer solutions.'

The choice of a layered velocity structure to describe the crust arose from one of the fundamental characteristics of explosion refraction travel time data. In general, such data can be fit quite well by a few straight-line segments, as can be seen in the data from station DW34 of *Shor et al.* [1970] in Figure 1. From the slopes of these straight lines, early marine seismologists could infer the seismic velocities of various zones within the earth which were not necessarily in contact with each other vertically. To determine the depth of each zone, it was necessary to assume velocities for the intervening regions in which the velocity was unknown. The simplest assumption was that each region of unknown velocity had the same velocity as an immediately overlying zone of known velocity. Although the net result of this procedure was a homogeneously layered velocity profile having as many layers as straight-line segments fit through the data, it is clear that the homogeneity of the observed 'layers' and the existence of interfaces between them are artifacts of the assumptions about the velocities in unobserved depth regions.

Many of the pioneer marine seismologists, such as *Ewing et al.* [1937, 1939], explicitly pointed out the assumption of layering. *Raitt* [1956] states:

> Calculation of the velocity-depth structure from the observed travel times was based on a simplified model of layers of constant velocity as determined from the travel-time plots . . . . This model represents a simplification of the actual situation, where velocities probably vary continuously with depth and possibly with horizontal distance, but it is a rough approximation and provides a basis for comparison of results.

In other early papers these assumptions were presumed to be known to the reader and were not stated explicitly.

Although we shall show that certain parameters of the traditional layered models are still useful, enough additional data have amassed to necessitate a significant refinement of our view of the oceanic crust. As was mentioned earlier, homogeneously layered velocity models can be used to fit the first arrival travel time data from a marine refraction profile very well. Such models are not the only models which will fit the data, however. For example, the travel time data from refraction station DW34 of *Shor et al.* [1970] are shown in Figure 1 along with the travel time curves from their layer solution and from the velocity profile for DW34 obtained by *Kennett and Orcutt* [1976]. The two velocity models are shown in Figure 2. Clearly, both models satisfy the data almost equally well, and they are in reasonable agreement on the

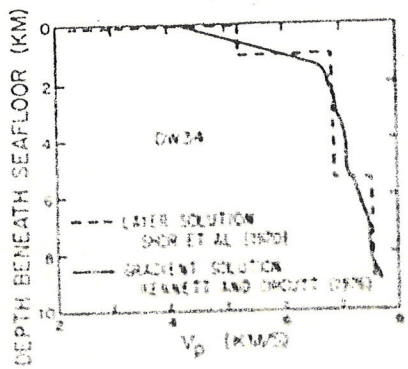

Fig. 2. Two rather different velocity profiles which fit the travel time data for DW34, shown in Figure 1

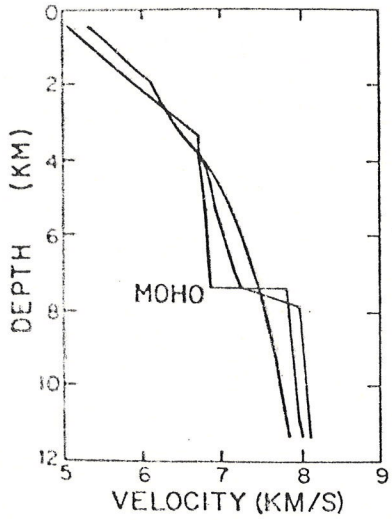

Fig. 3. Three velocity profiles which fit the observed travel times of the *P* waves in Figure 4. Note the different Moho transitions at 8-km depth. Depth is measured from the top of the crust.

One interesting development: upper mantle beneath oceanic Moho is <u>anisotropic</u>

In isotropic mantle, Moho head wave would have same velocity in all directions.

Observation

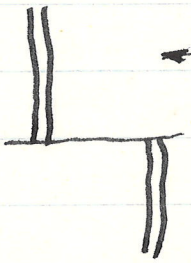

$\alpha \sim 5-7\%$ faster in direction parallel to spreading

Data from Morris thesis.
Process of crustal creation at ridge somehow aligns olivine xtals non-randomly.

There have also been long refraction lines shot on land, e.g. away from NTS or Lake Superior experiment clear across US

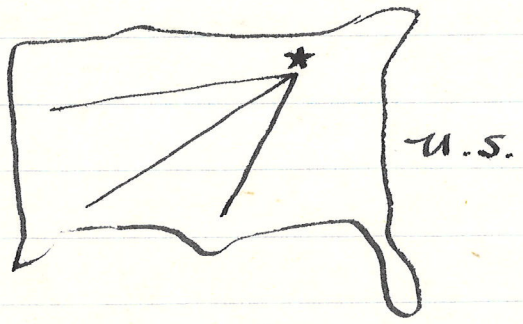

lines > 1000 km long,
very large explosions, see refractions from 400-600 km deep.

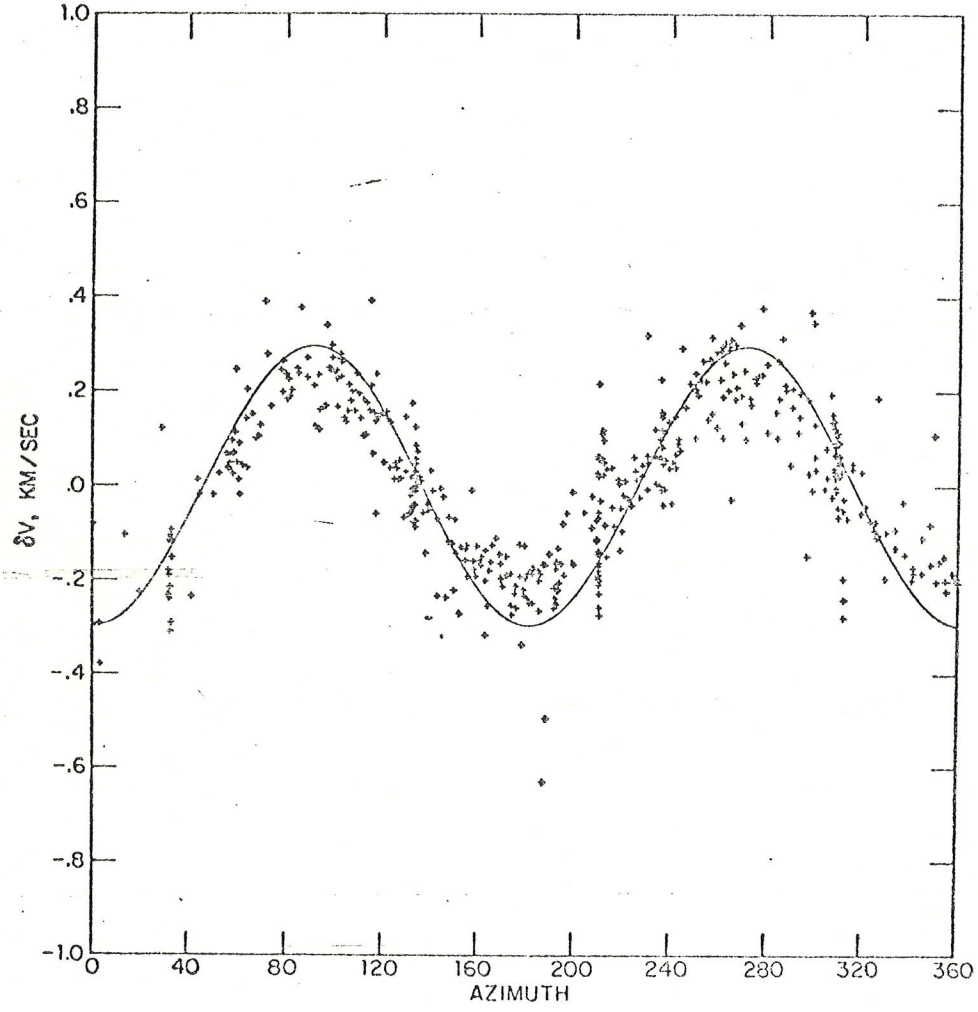
1.0
.8
.6
.4
.2
.0
-.2
-.4
-.6
-.8
-1.0
δV, KM/SEC
0
40
80
120
160
200
240
280
320
360
AZIMUTH

Seismometers: about which we say almost nothing.

Box 3:

The nature of the wiggly line influenced strongly by instrument response.

Ideal seismometer would employ a skyhook. Want to measure motion or displacement of ground at a point on ⊕'s surface

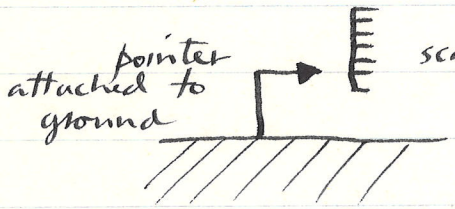

the ideal vertical seismometer

Actual seismometers are all some variation of a mass on a spring, e.g. Sprengnether vertical deployed in basement of Guyot Hall. There are also horizontal seismometers.

Crustal profiling work uses geophones on land and hydrophones (respond to changes in water pressure) at sea.

Seismometers used in global seismology of 3 basic types:

1. short period: response peaked about 1 s, typically, useful for accurate timing of arrivals

2. long-period: peaked around 10–30 s typically, these waves longer wavelength, less subject to scattering off small irregularities, many details of waveforms easier to interpret and understand, also useful for studying surface waves.

3. ultra-long period: strain meters and gravity meters, record ⊕ tides, also long-period free oscillations of ⊕ and surface waves.

WWSSN: a world-wide network of identical short- and long-period instruments, data available on microfiche film chips, we shall look at this kind of data (long-period) in lab.

MANUFACTURERS·OF
·SEISMOLOGICAL·GEOPHYSICAL·AND·ENGINEERING·INSTRUMENTS···4567·SWAN·AVE·

W. F. SPRENGNETHER INSTRUMENT CO. INC.

·SAINT·LOUIS·MO·63110·U·S·A·
Telephone: 314-535-1682
Cable: SPRENCO

- *Spring Resonance above 20 Hz*
- *Excellent Period and Coil Constant Invariance With Boom Position and Amplitude*
- *Independent Calibration Coil*
- *Displacement Transducer*

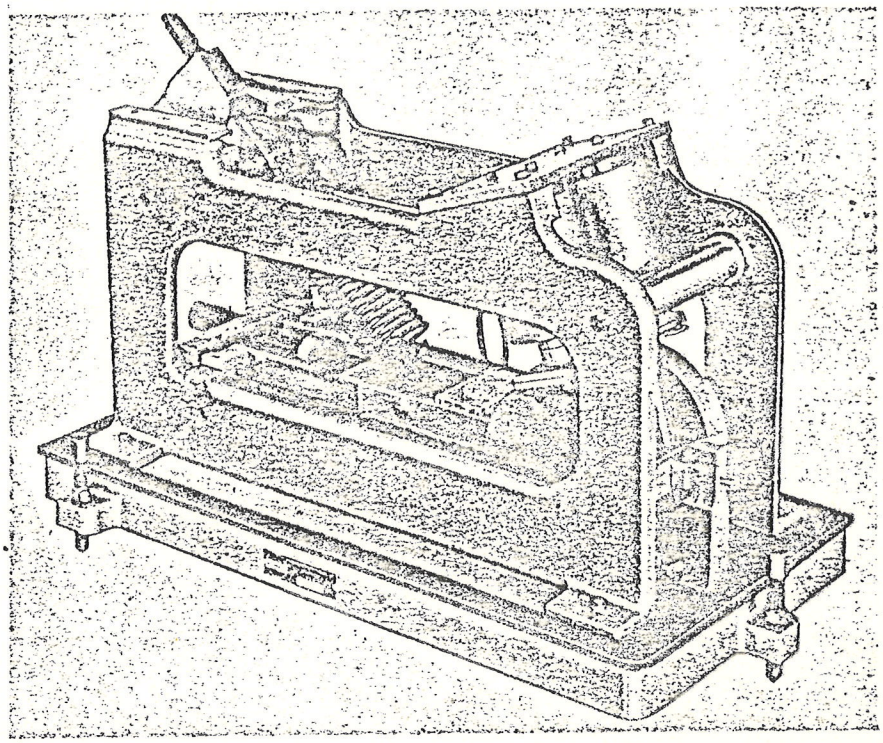

SPRENGNETHER

HIGH PERFORMANCE LONG PERIOD VERTICAL SEISMOMETER

S-5100-V

The Sprengnether model S-5100-V has been developed specifically to overcome difficulties experienced when operating standard long period vertical seismometers in unconventional applications (i.e. other than with long period galvanometers) requiring large bandwidth or gain. Examples are: broadband recording (0-20 Hz); very high gain narrow band systems (1-5 Hz short period, 5-15 Hz high frequency, 20-40 sec. surface wave); or accurate large motion measurement (2 mm range with less than 5% variation in response parameters).

The instrument resulting from studies of these problems is a long period vertical seismometer at unequalled performance specifications. Basically, the excellent independence of natural period and transducer sensitivity upon boom position characteristic of the S-5007-V has been retained, while factors adversely affecting performance in the special applications have been removed.

Continued on reverse side.

RESPONSE OF SEISMOMETER - AMPLIFIER COMBINATIONS

OUTPUT OF AMPLIFIER FOR 100 mμ ground motion

(WITH 33db attenuator AND RECORDER GAIN EQUAL TO 30)

MAGNIFICATION OF GROUND MOTION

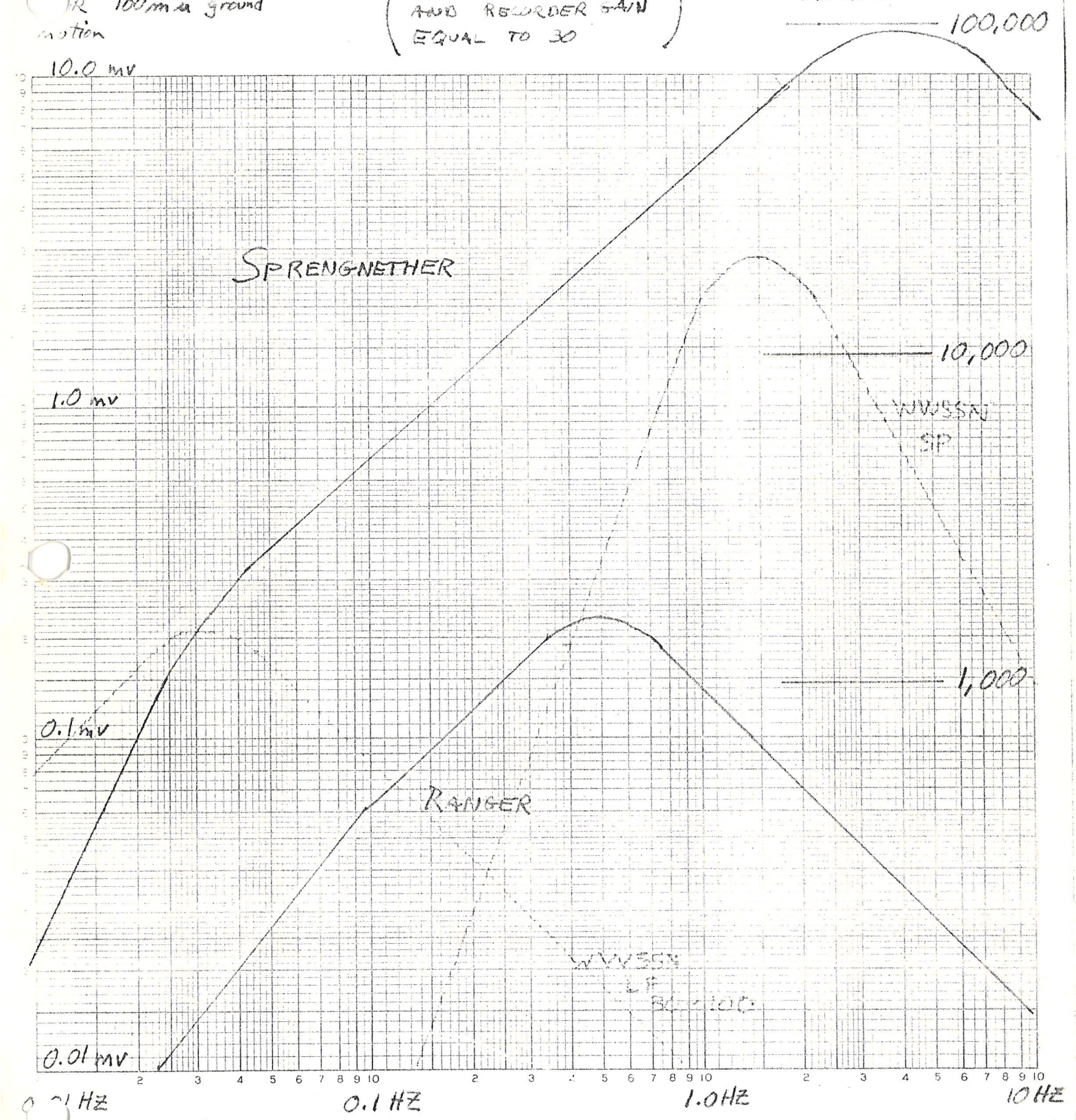

Wiechert - Herglotz inversion : we shall follow Bullen, the method is evidently due to Rasch. See Appendix D of Stacey.

Assume : $p(\Delta)$ is a known function.

Assume : $\eta(r) = r/v(r)$ decreases monotonely as r decreases, i.e.

$$d\eta/dr > 0 \quad \text{or}$$

$$dv/dr < v/r$$

Find : the velocity structure $v(r)$.

i.e. we assume the structure is such that a ray bottoms at every depth of interest. The method fails if that is not true, we'll discuss later how to deal with this failure.

$$\eta = r/v$$

$$d\eta/dr = \frac{1}{v} - \frac{r}{v^2}\frac{dv}{dr} > 0 \rightarrow \frac{dv}{dr} < \frac{v}{r}.$$

We assume $p(\Delta)$ has been measured, can be done directly using arrays or by numerical differentiation of $T(\Delta)$.

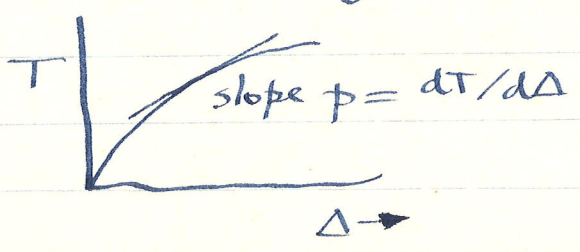

In practice one must somehow smooth and interpolate discrete observations of $T(\Delta)$.

not a necessary assumption.

For simplicity we shall assume surface focus. Then we know that for a ray with parameter p

$$T(p) = 2\int_{r_p}^{a} \frac{\eta^2\, dr}{r(\eta^2 - p^2)^{1/2}}$$

$$\Delta(p) = 2\int_{r_p}^{a} \frac{p\, dr}{r(\eta^2 - p^2)^{1/2}}$$

} solution to direct problem for any model $v(r)$.

this is where we use the assumption.

If $\eta(r)$ is monotone can be inverted for $r(\eta)$ and we can change variables in formula for Δ:

$$\star\quad \Delta = 2\int_{\eta_p}^{\eta_a} \frac{p}{r}(\eta^2 - p^2)^{-1/2} \frac{dr}{d\eta}\, d\eta$$

$$\eta_a = a/v(a)$$

$$\eta_p = r_p/v(r_p) = p$$

since $\sin i = 1$ at turning pt.

Let r_1 be a given depth where one wishes to find $v(r_1)$. We shall find $v(r_1)$ for an arbitrary r_1 by an explicit formula (this very rare in geophysical inverse problems).

Let Δ_1 be Δ for ray which <u>bottoms</u> at r_1

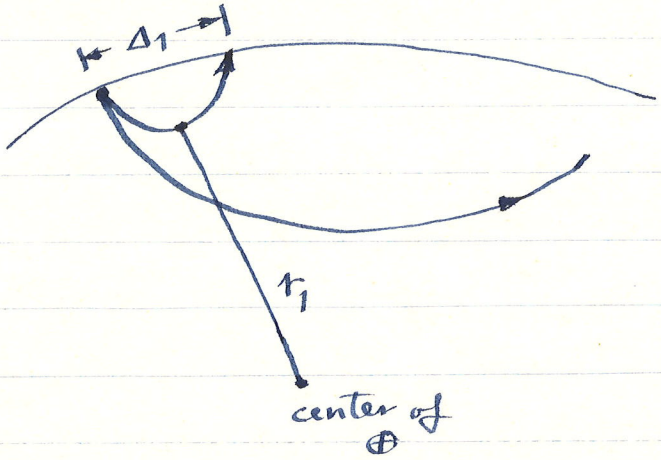

Apply the operator $\int_{\eta_1}^{\eta_a} d\rho\,(\rho^2-\eta_1^2)^{-1/2}$

to both sides of ★ $(\eta_1 = \eta_1(v(r_1)))$

$$\int_{\eta_1}^{\eta_a} \Delta(\rho^2-\eta_1^2)^{-1/2}\,d\rho$$

$$= \int_{\eta_1}^{\eta_a} d\rho \int_{\eta_\rho}^{\eta_a} \frac{2\rho}{r}\left[(\rho^2-\eta_1^2)(\eta^2-\rho^2)\right]^{-1/2}\frac{dr}{d\eta}\,d\eta$$

$\eta_\rho = \rho$.

Integrate the l.h.s. by parts:

$$u = \Delta$$

$$dv = (\rho^2-\eta_1^2)^{-1/2}\,d\rho$$

$$du = \frac{d\Delta}{d\rho}\,d\rho$$

$$v = \cosh^{-1}(\rho/\eta_1)$$

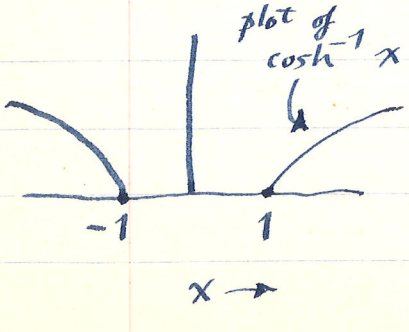

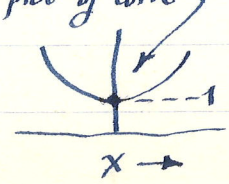

"arc cosh"

this argument is always ≥ 1 for $\eta_1 \leq \rho \leq \eta_a$ (because ρ is a decreasing fcn of Δ)

$$\left[\Delta \cosh^{-1}\left(\frac{\rho}{\eta_1}\right)\right]_{\eta_1}^{\eta_a} - \int_{\eta_1}^{\eta_a} \frac{d\Delta}{d\rho} \cosh^{-1}\left(\frac{\rho}{\eta_1}\right) d\rho$$

this term vanishes since:

1. $\Delta = 0$ when $\rho = \eta_a$ (the ray that leaves source horizontally)
2. $\cosh^{-1}(\rho/\eta_1) = 0$ when $\rho = \eta_1$.

Now change variables from ρ to Δ in the integral.

$\rho = \eta_a$: $\Delta = 0$ i.e. $\rho(0) = \eta_a$

$\rho = \eta_1$: $\Delta = \Delta_1$ i.e. $\rho(\Delta_1) = \eta_1$

Get on l.h.s.

$$\int_0^{\Delta_1} \cosh^{-1}\left(\frac{\rho}{\eta_1}\right) d\Delta$$

$\rho(\Delta_1)$

Now consider r.h.s. interchange order of integration. Recall $\eta_\rho = \rho$ (lower limit of integral over η. The region of integration thus looks like.

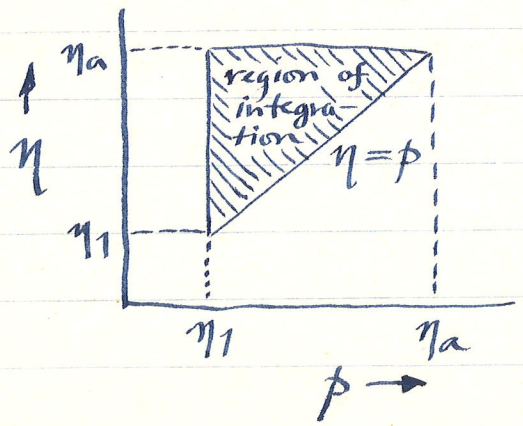

Thus get, upon interchange,

$$\int_{\eta_1}^{\eta_a} d\eta \int_{\eta_1}^{\eta} \frac{2p}{r}\left[(p^2-\eta_1^2)(\eta^2-p^2)\right]^{-1/2} \frac{dr}{d\eta}\, dp$$

$\frac{dr}{d\eta}$ does not depend on p (take outside)

$$= \int_{\eta_1}^{\eta_a} d\eta \, \frac{dr}{d\eta} \underbrace{\int_{\eta_1}^{\eta} \frac{2p}{r}\left[(p^2-\eta_1^2)(\eta^2-p^2)\right]^{-1/2} dp}$$

this integral can now be carried out, in fact

$$\int_{\eta_1}^{\eta} p\left[(p^2-\eta_1^2)(\eta^2-p^2)\right]^{-1/2} dp = \pi/2 \quad , \text{ for } \eta > \eta_1 .$$

hence $$= \int_{\eta_1}^{\eta_a} \frac{\pi}{r} \frac{dr}{d\eta}\, d\eta$$

$$= \pi \int_{r_1}^{a} \frac{dr}{r} = \pi \ln\left(\frac{a}{r_1}\right)$$

We have thus shown that

$$\pi \ln\left(\frac{a}{r_1}\right) = \int_0^{\Delta_1} \cosh^{-1}\left(\frac{p(\Delta)}{p(\Delta_1)}\right) d\Delta$$

this argument will be greater than 1 if p is a decreasing fcn. of Δ as it is in the lower mantle

By assumption $p(\Delta)$ is known for $0 < \Delta < \Delta_1$

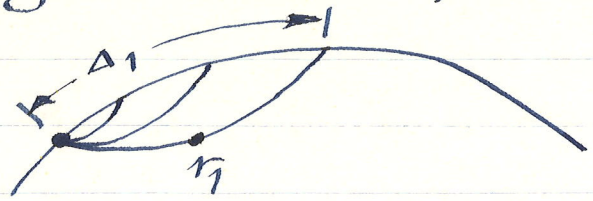

Thus we solve for r_1, bottoming depth of ray emerging at distance Δ_1. Then

$v(r_1) = r_1 / \eta_1 = r_1 / p(\Delta_1)$

$$\boxed{v(r_1) = r_1 / p(\Delta_1)}$$

We can use this algorithm to work our way down the $p(\Delta)$ curve. This yields a unique velocity profile $v(r)$. We work our way down from the surface.

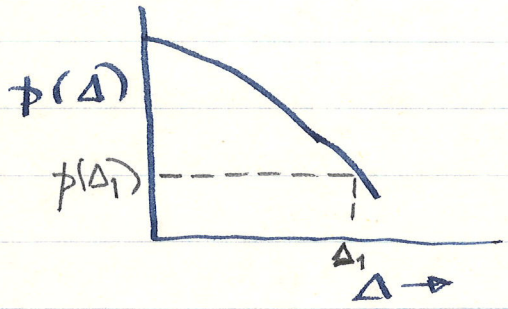

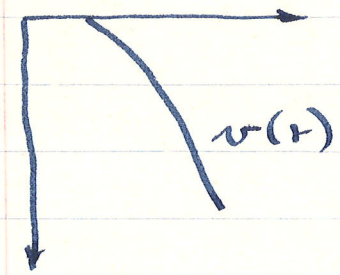

The method only works down to the top of the first LVZ, i.e. fails at first depth where no ray bottoms.

Let's forget for the moment about upper mantle LVZ.

What about a triplication?
Answer: method works fine if $p(\Delta)$ is known, including on the back branch

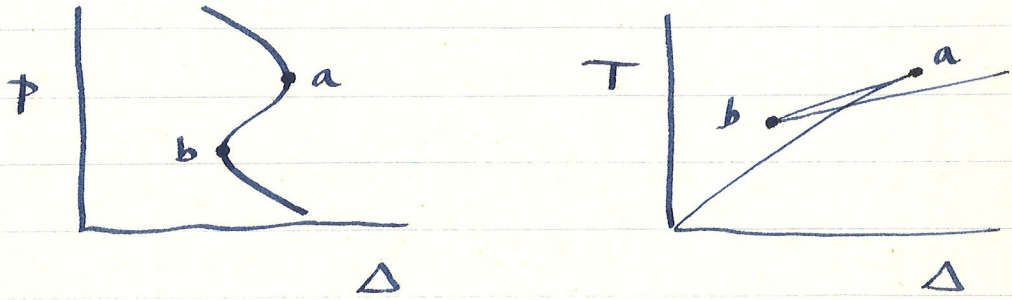

If the later arrivals have been picked and $p(\Delta)$ the method works as before, only difference is that $d\Delta$ must be taken negative on back branch from a to b.

What about a sudden increase e.g. SKS, $\beta_{mantle} \sim 7.2$ km/s, $\alpha_{core} \sim 8.0$ km/s.

Method still works fine. Way it is applied to core in practice.

One first determines $\beta(r)$ in mantle down to core mantle bdry.

Then mantle contribution to $T(\Delta)$ can be explicitly computed. A new curve $T'(\Delta')$ for K in the core only can be determined by subtraction.

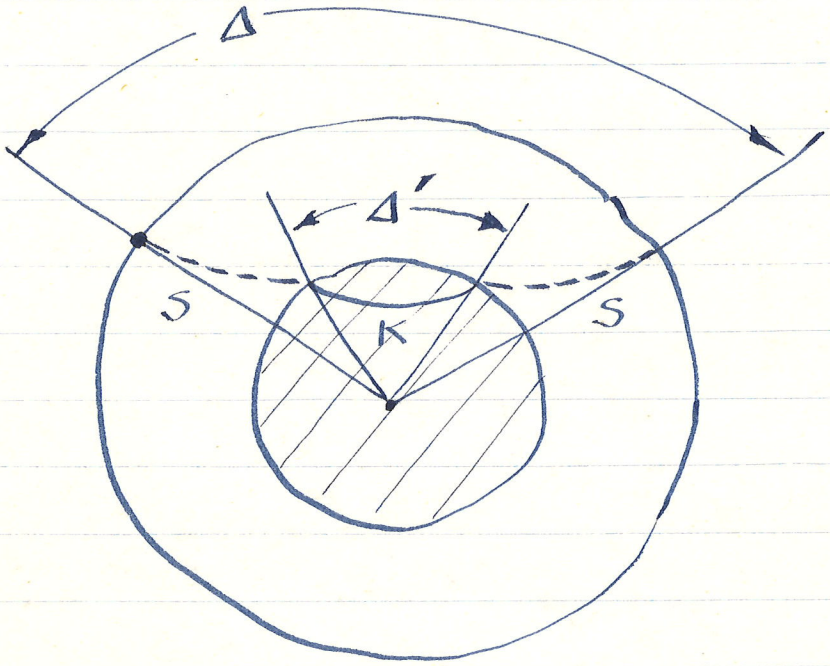

Then the Wiechert-Herglotz procedure is applied to $T'(\Delta')$ for K in the core to find $\alpha(r)$ in the core. This process is called "stripping the mantle".

Note: it is SKS, SKKS etc. which enable us to determine $\alpha(r)$ in the core as they bottom at every depth, whereas PKP does not.

How does one handle the LVZ in the upper mantle?

The classical approach is to assume a reasonable structure, then strip it and proceed as before.

For example, the various LVZ structures considered by Lane Johnson to invert his TFSO $\chi(\Delta)$ data shown in Fig. 6.

Note: this practice destroys the uniqueness of the model below as well, since one's answer now depends on the assumed LVZ structure.

As we shall see later, surface wave dispersion studies can be used to help constrain the LVZ.

The classical approach (WH inversion combined with stripping) had by ~1930's led to a pretty good picture of $\alpha(r)$ and $\beta(r)$ in the mantle + core, largely through the work of Sir Harold Jeffreys and K.E. Bullen.

A modern approach: due to Gerver and Marcushevitch and others.

It has recently become clear that the natural variable to use in such studies is neither $p(\Delta)$ nor $T(\Delta)$ but rather

$$\tau(p) = T(p) - p\,\Delta(p)$$

- τ: units of time
- T: travel time of ray with parameter p
- Δ: distance travelled by ray with parameter p

If both $T(\Delta)$ and $p(\Delta)$ are known then $\tau(p)$ can easily be determined.
A plot of $\tau(p)$ for S, SKS and ScS and for P, PKP and PcP is shown in Fig. 12.9, originally from Johnson + Gilbert, this calculated directly from J-B tables, or an updated version thereof.

~~The general form of such a plot~~

Recall for a surface source

$$T = 2\int_{r_p}^{a} \frac{\eta^2\,dr}{r(\eta^2-p^2)^{1/2}} \qquad \Delta = 2\int_{r_p}^{a} \frac{p\,dr}{r(\eta^2-p^2)^{1/2}}$$

note $\frac{1}{\sqrt{\ }}$ singularity

But note that

$$\tau(p) = T(p) - p\,\Delta(p) = 2\int_{r_p}^{a} \frac{dr}{r}\left(\eta^2 - p^2\right)^{1/2}$$

no singularity

This is just one of the many nice features of the new datum $\tau(p)$. Another is that it "automatically" irons out triplications.

Can be shown that considered as a function of Δ, τ is the intercept on the T axis of the tangent to the $T(\Delta)$ travel-time curve

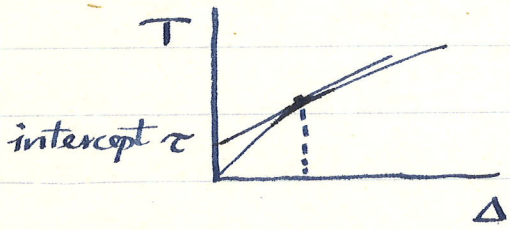

A plot of $T(\Delta)$ at a triplication looks like:

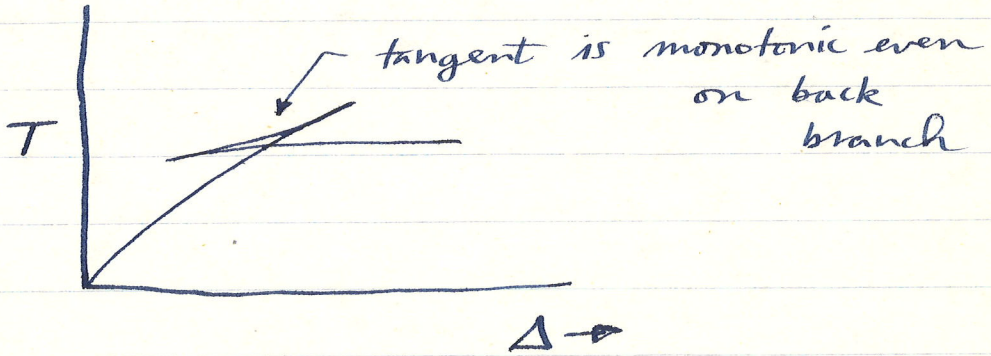

Thus $\tau(\Delta)$ has no triplication

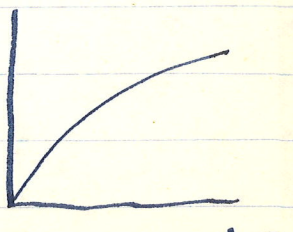

Another property of a $\tau(p)$ plot is that

$$d\tau(p)/dp = \frac{d}{dp}[T - p\Delta]$$

$$= \frac{dT}{dp} - \Delta - p\frac{d\Delta}{dp}$$

$$= \frac{dT}{dp} - \Delta - \frac{dT}{d\Delta}\frac{d\Delta}{dp} = -\Delta$$

[cancel ⟶]

Thus $\boxed{d\tau(p)/dp = -\Delta(p)}$

The slope of τ vs. p is thus just $-\Delta$. Furthermore $-\Delta(p)$ is always a single-valued function of $-p$.

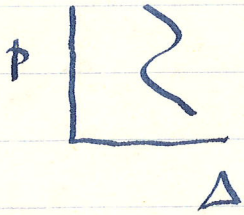

$p(\Delta)$ is triple-valued if there is a triplication, but $\Delta(p)$ is single-valued.

Thus $\tau(p)$ is monotonically decreasing and single-valued.

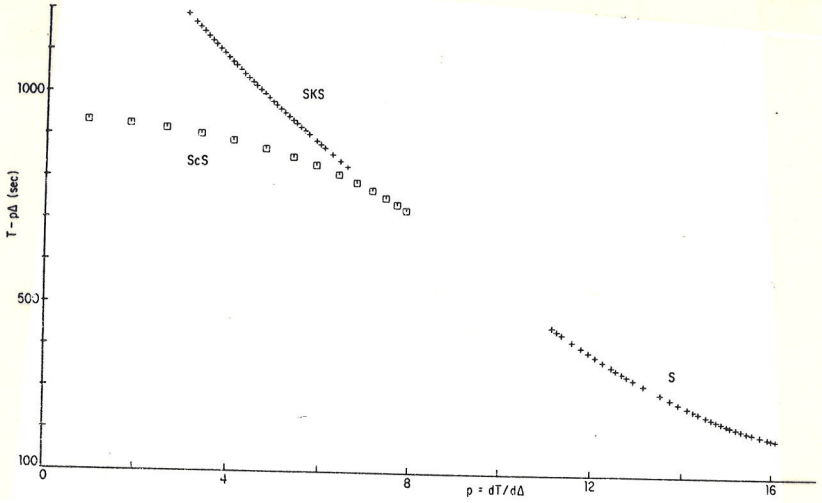

FIG. 5. $\tau(p)$ for the teleseismic data S, ScS, SKS, p in sec/deg.

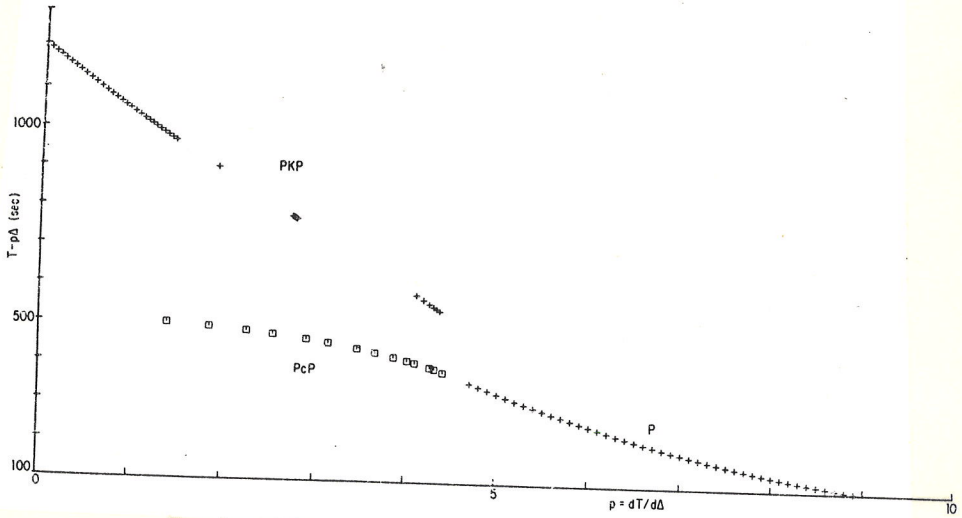

FIG. 4. $\tau(p)$ for the teleseismic data P, PcP, PKP, p in sec/deg.

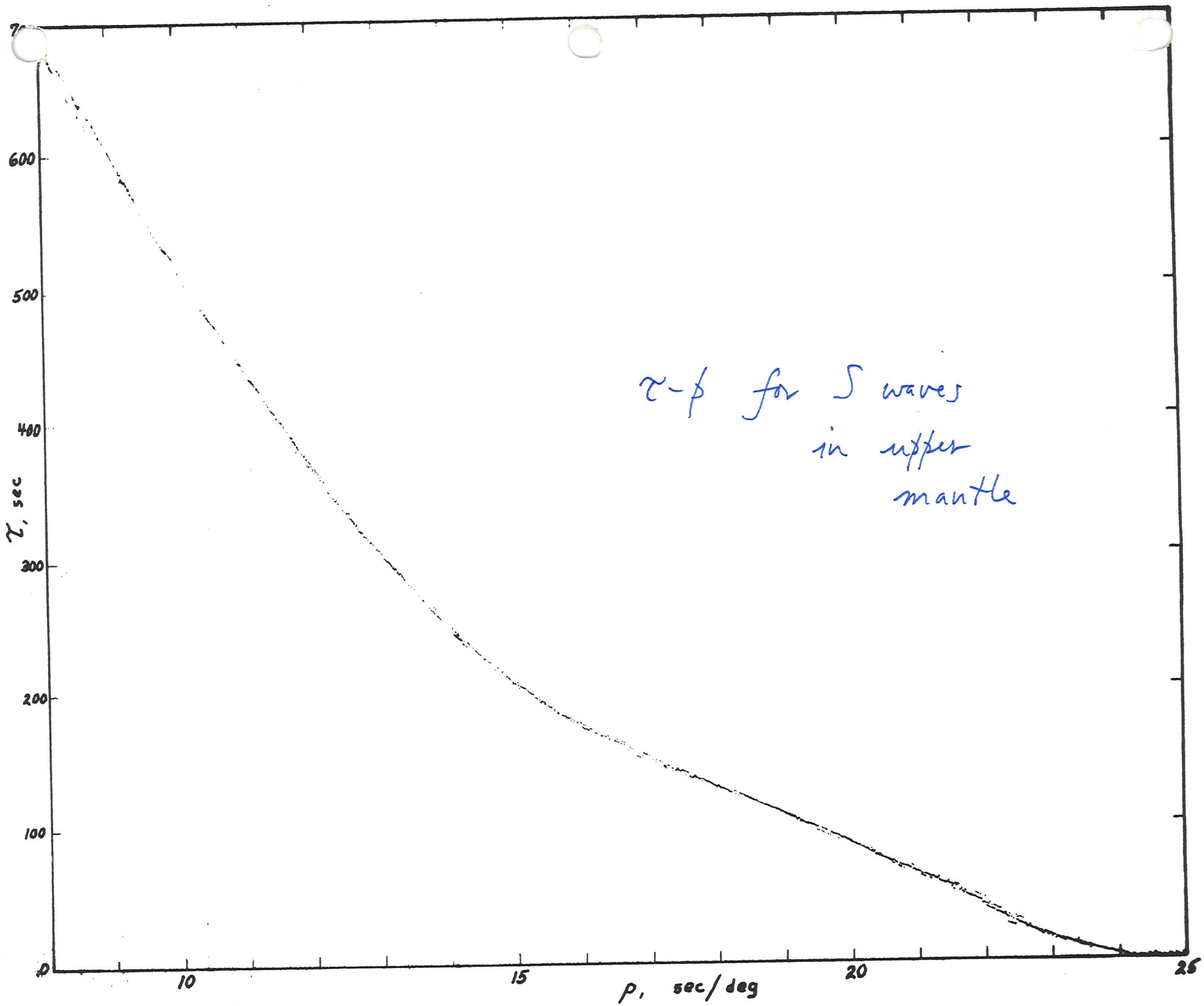

Figure 3. A simple slant-stack for the data in Figure 2. For each value of slowness p the tau value corresponding to the largest number of travel times is plotted.

Consider the case of S, ScS and SKS.
T vs. Δ looks like

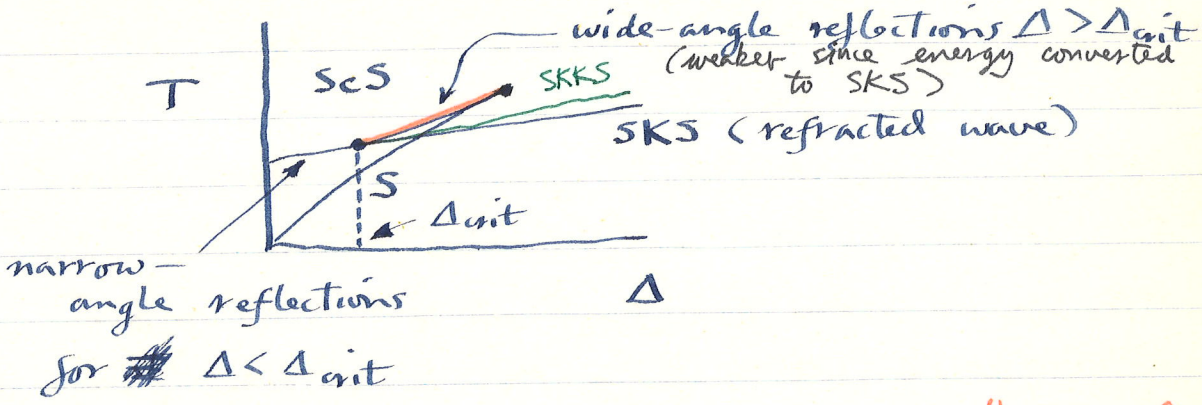

Thus τ vs. p looks like

these suffer total internal reflection

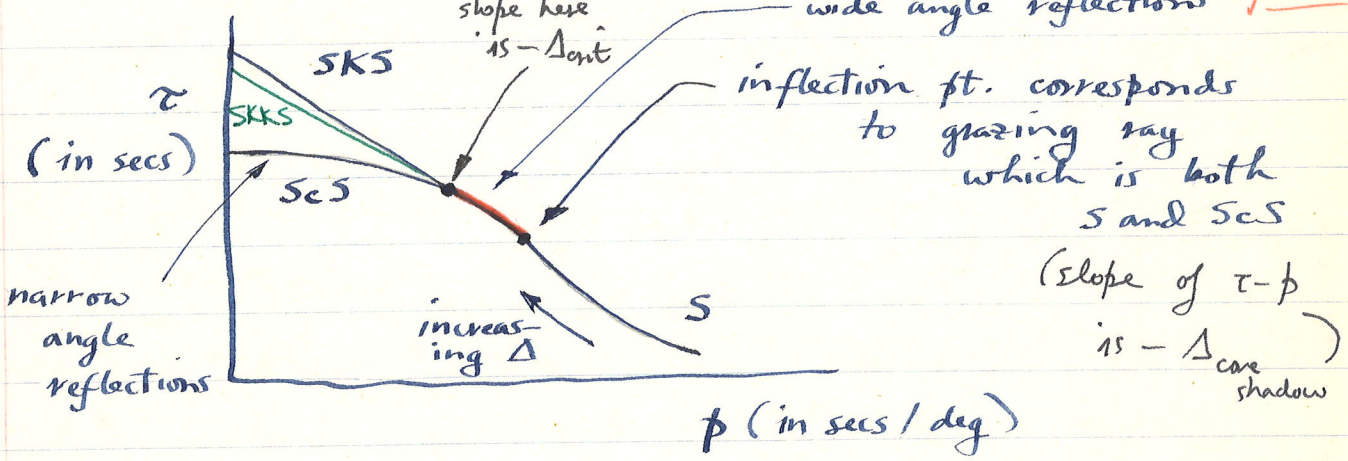

The P, PcP and PKP case looks like:

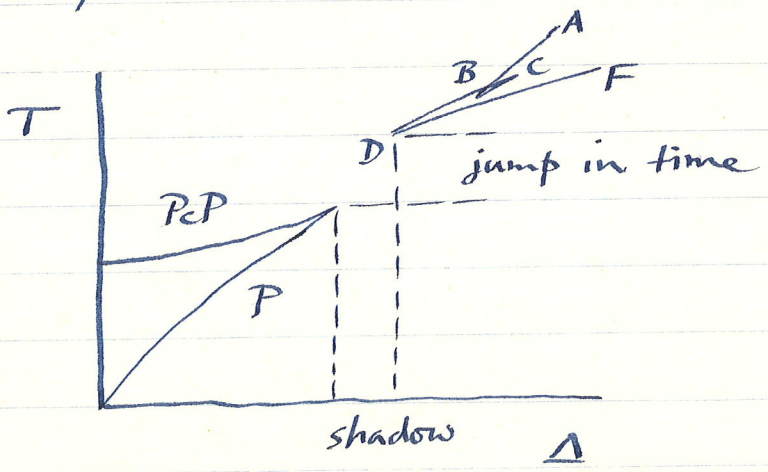

Then $\tau(p)$ looks like

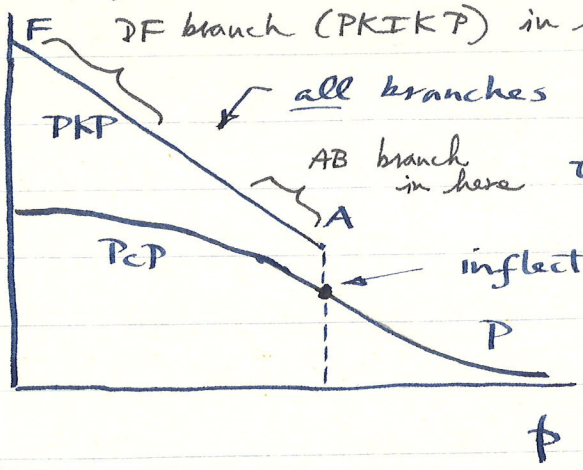

Why does all of PKP plot along a monotonic curve in τ-p plot?

Because

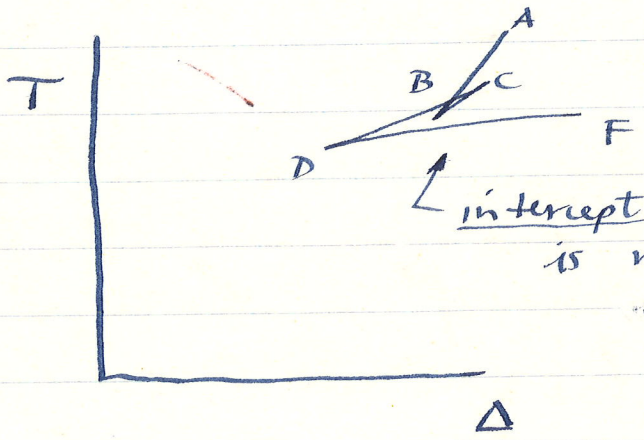

The formal results of τ-p inversion obtained by Gerver + Markushevich take the following form:

If $\exists$ an LVZ what can be determined uniquely? Recall: if no LVZ all of $v(r)$ is unique.

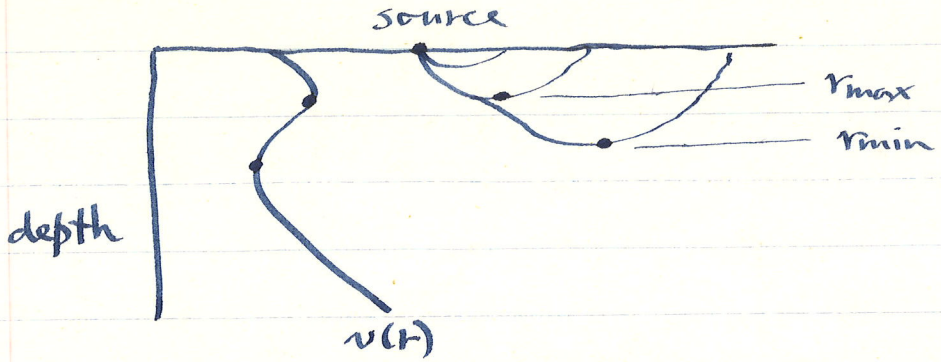

Using data from surface focus events only, $v(r)$ is unique down to r_{max}, $\exists$ upper bound in LVZ and both an upper and lower bound below LVZ, i.e.

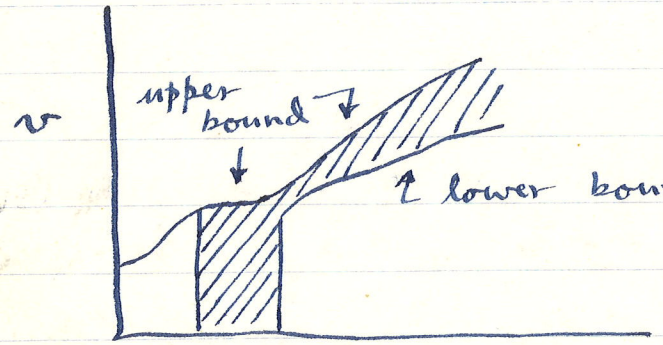

Not every curve in shaded region is a soln but a solution can be found passing thru any pt.

If $\exists$ 2 LVZ's get a "giraffe" plot comme ça

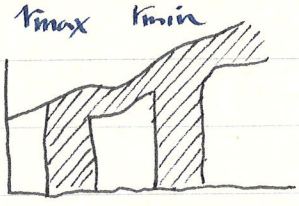

If one selects a soln in LVZ then soln below is unique (can be obtained by stripping)

Using complete data from an event below LVZ as well : v

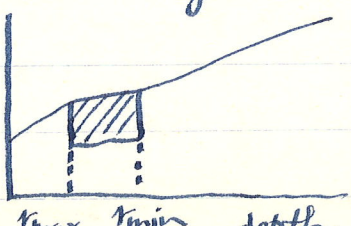

above + below LVZ now unique, also $\exists$ upper and lower bound in LVZ.

The use of travel time residuals to study geographical variability

The P and S velocity structure of the spherically averaged ⊕ is no longer a matter of great concern.

Modern travel time studies make use of JB residuals, such as those you measure in the lab, to look for and study deviations from spherical symmetry, or geographical variability. Demands corrections for ⊕'s ellipticity, station elevations, etc. We briefly cite 2 examples of this kind of work:

1. Soon after development of plate tectonic hypothesis, it was realized that cold subducted slabs should faster than their surroundings (noted in lab that $d\alpha/dT$ and $d\beta/dT$ negative, cold → more rigid → faster) One would thus predict:

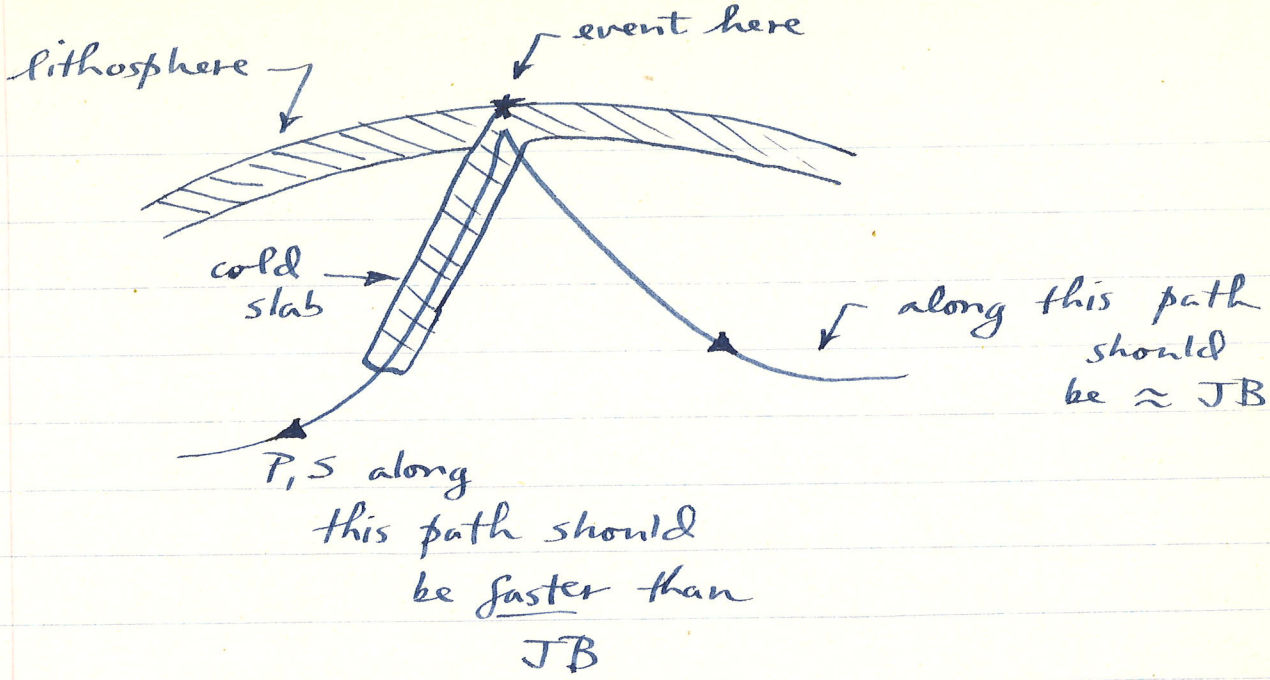

Thermal models suggest that α should be a few percent faster in the slab so that the residuals should be a few seconds

This phenomenon was sought for and found, first by Davies + McKenzie using nuclear explosions (time + location known precisely) in Aleutians.

Question: how deep do the slabs penetrate? Deep focus seismicity, a manifestation of thermal equilibration process ceases at 600–650 km depth but thermal modeling suggests that cold slab should protrude deeper.

An attempt to answer this question:
Jordan 1977: used a deep focus quake

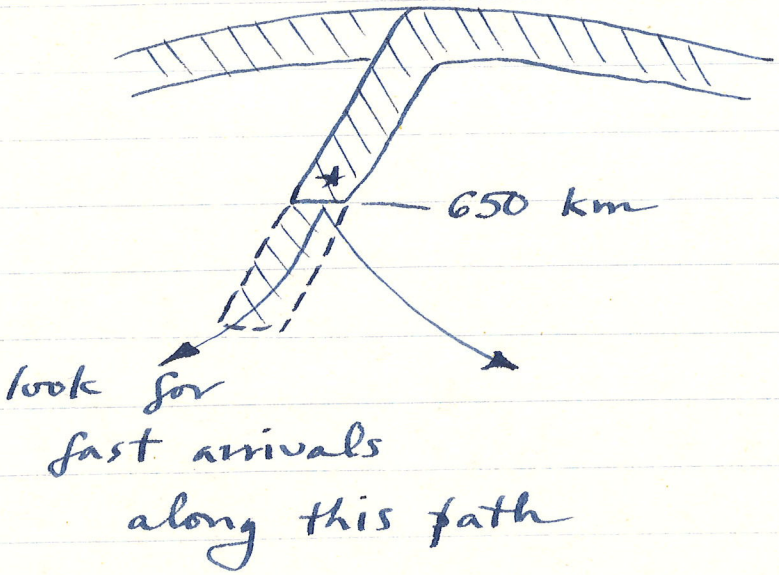

Fig. 1 shows cross-section of Kurile-Kamchatka seismicity, ends at 650 km depth, and event used.
Fig. 5 shows stereographic projection of residuals plotted on focal sphere, after allowance for station anomalies (mean residual of all events at a given station: a measure of local crustal structure under station).

Ignore dotted lines (used to define a portion of focal sphere projected in a different projection for another figure).

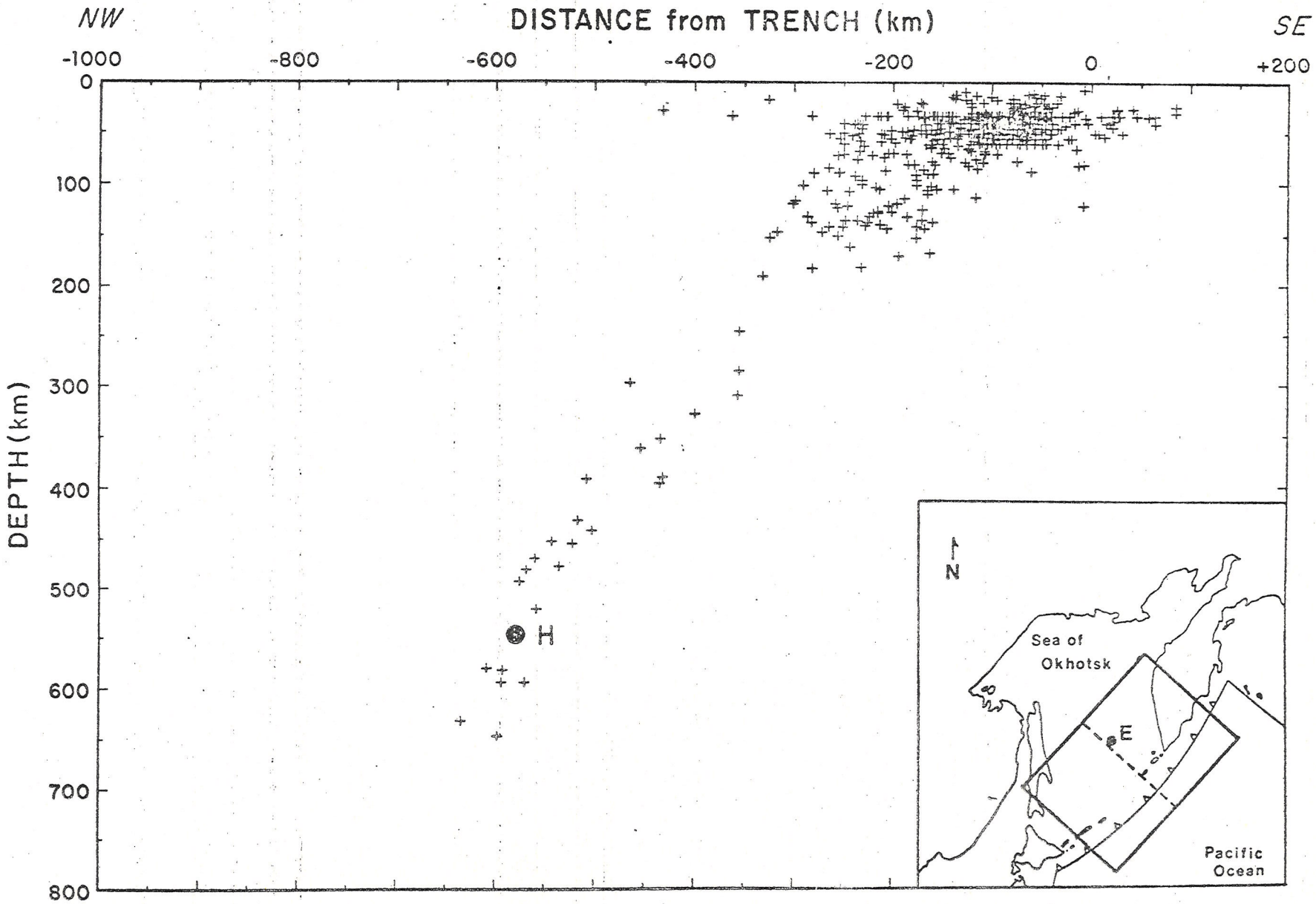
NW
DISTANCE from TRENCH (km)
SE
-1000
-800
-600
-400
-200
0
+200
DEPTH (km)
0
100
200
300
400
500
600
700
800
H
N
Sea of
Okhotsk
E
Pacific
Ocean

FIGURE 1

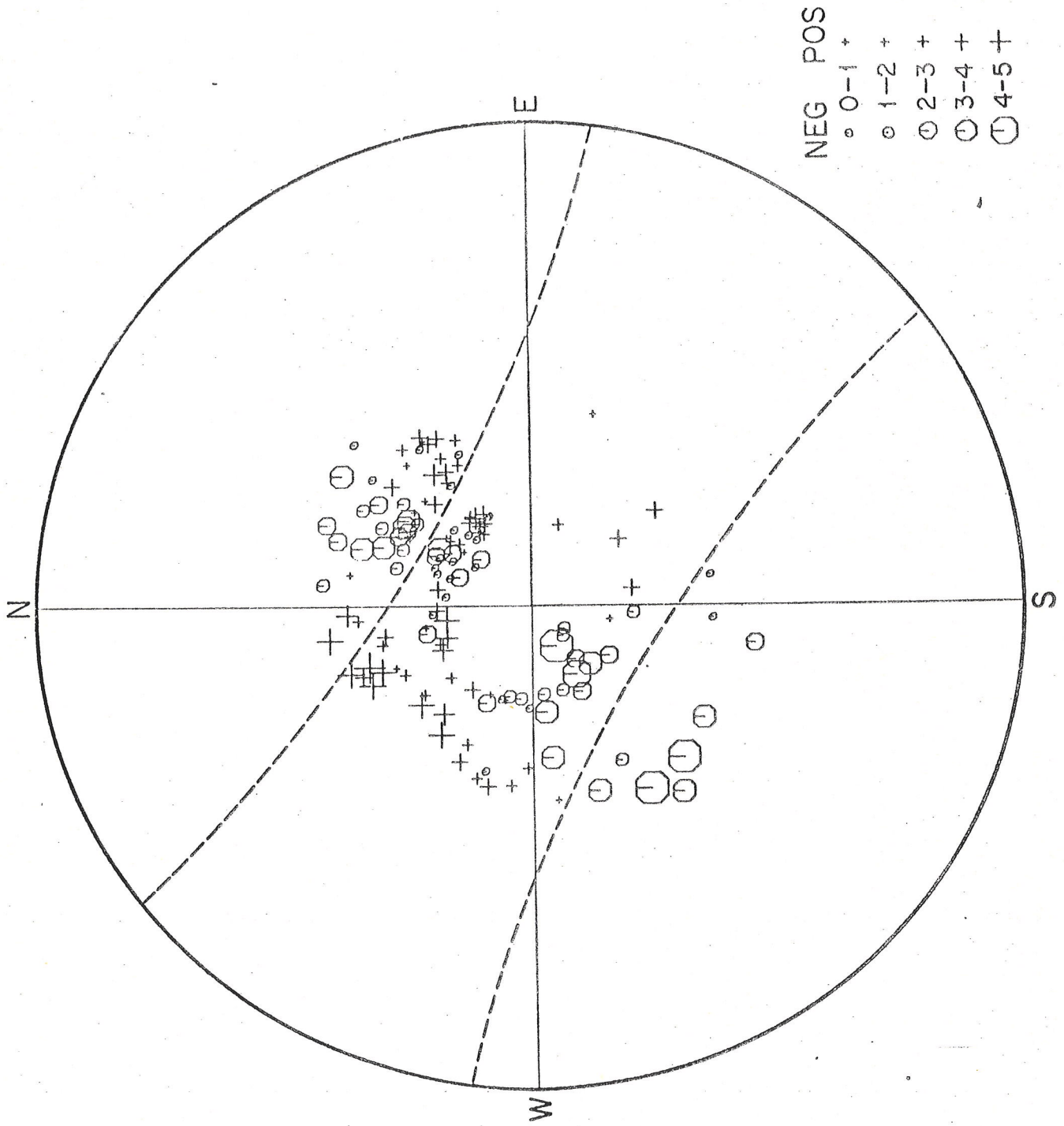

FIGURE 5

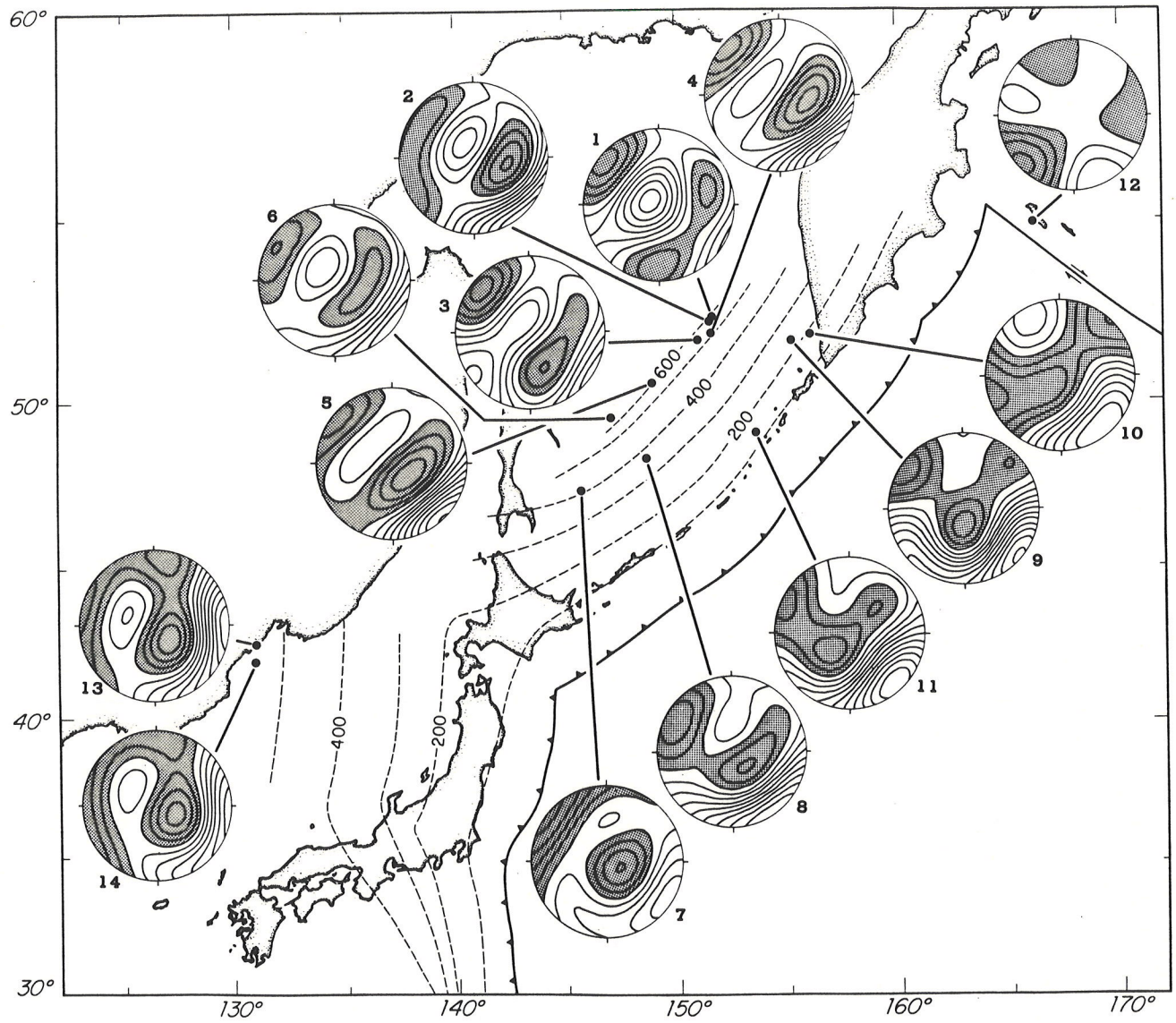

Fig. 3. Earthquakes epicenters (solid circles) and smoothed residual sphere diagrams on a Mercator projection of the northwest Pacific. Pacific plate boundary (heavy solid line) and seismicity contours in kilometers (dashed lines) are indicated. Smoothed residual spheres are the middle diagrams of Figure 2, annotated by the event numbers of Table 1.

Jordan suggests the data is characterized by a NE–SW trough of negative residuals (negative ≡ faster than JB)

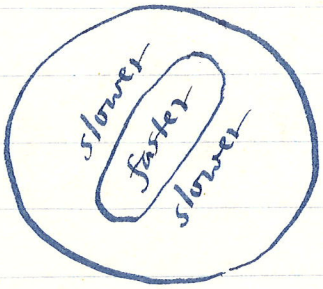

You are invited to see if you agree.

Note from Fig. 1 strike of subduction zone is NE–SW. Jordan concludes the slab penetrates to ~ 1000 km depth with a velocity contrast of 5%.

2. Sipkin-Jordan study of ScS and multiple ScS:

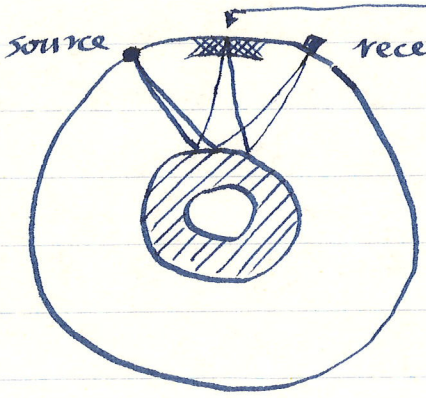

Ray paths for ScS and ScS2

Note that near-source and near-receiver anomalies tend to cancel.

They studied the differential travel-time $T_{ScS2} - T_{ScS}$. As a general rule, lateral heterogeneity tends to be greater in uppermost few hundred kilometers.

$T_{ScS2} - T_{ScS}$ thus can tell one something about structure at <u>bounce point</u> at ⊕'s surface of ScS ⨯ in picture.

What would one <u>predict</u> for bounce <u>points</u> in the oceans?

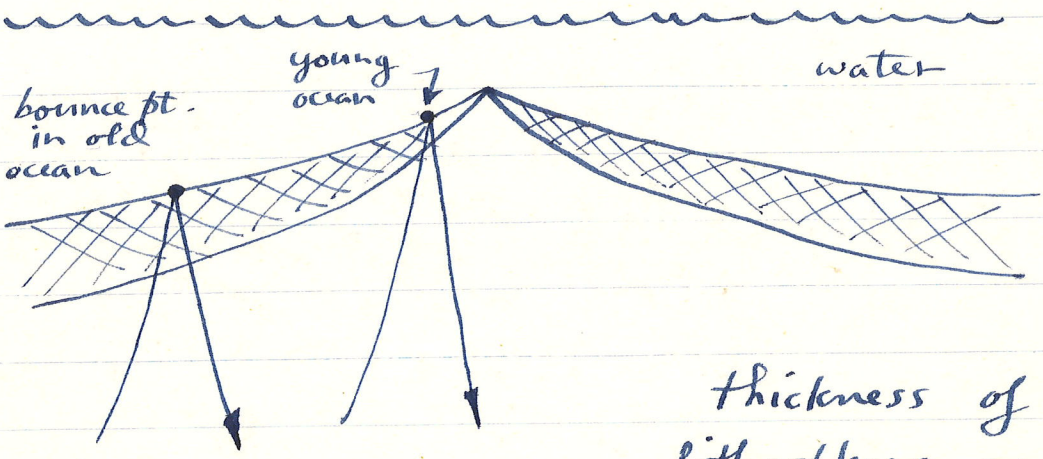

thickness of lithosphere ~ $\sqrt{age}$

$(ScS)_{SH}$ is employed to avoid P conversion problems, can't propagate in H_2O, bounce "pt." is ocean floor.

In old ocean wave traverses <u>more cold fast lithosphere</u> ⟹ should be faster. We would <u>predict</u>

$$T_{ScS2} - T_{ScS} \sim 1/\sqrt{age}$$

Fig. 12 shows some data plotted vs.

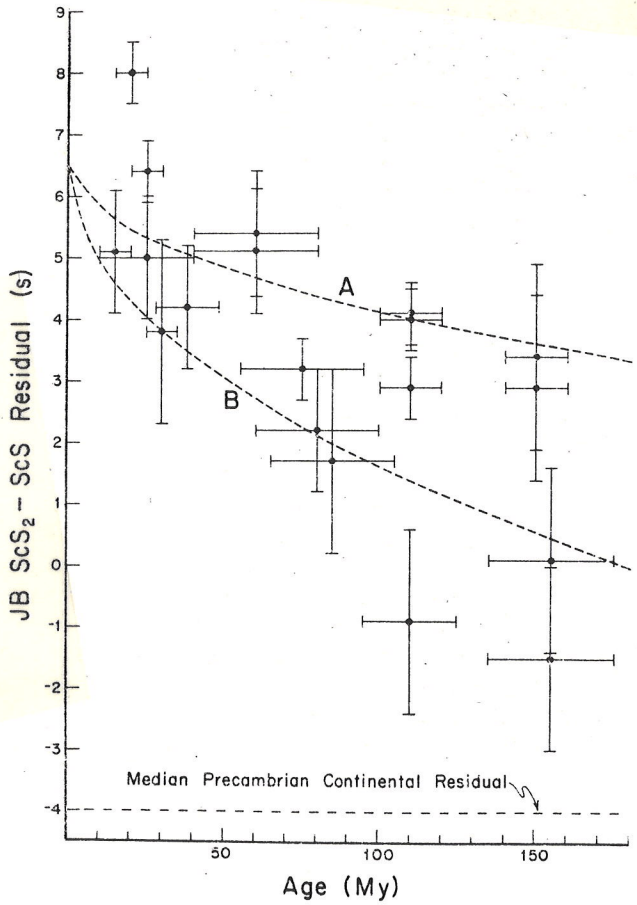

Fig. 12. Oceanic JB ScS_2-ScS residual versus crustal age at the surface reflection point of ScS_2. The error bars are subjective uncertainties. Curves A and B are explained in the text.

age. The dotted lines are two "theoretical" curves based on models of the velocity structure vs. age which fit surface wave dispersion data, both dotted curves ~ $\sqrt{\text{age}}$. Our prediction is seen to be fairly well substantiated.

They also compared residuals for ocean basins with residuals for continents. The results of this study summarized in histograms in Figs. 3 and 4.

~~Continental $T_{ScS_n} - T_{ScS_{n-1}}$~~

They have identified and studied ScS4, ScS3, etc. as well.

Continental $T_{ScS_n} - T_{ScS_{n-1}}$ is about -1 sec, faster than JB, while average ocean is about $+4$ sec, slower than JB.

They have used this to argue for deep-seated ocean-continent differences (cold fast roots under continents).

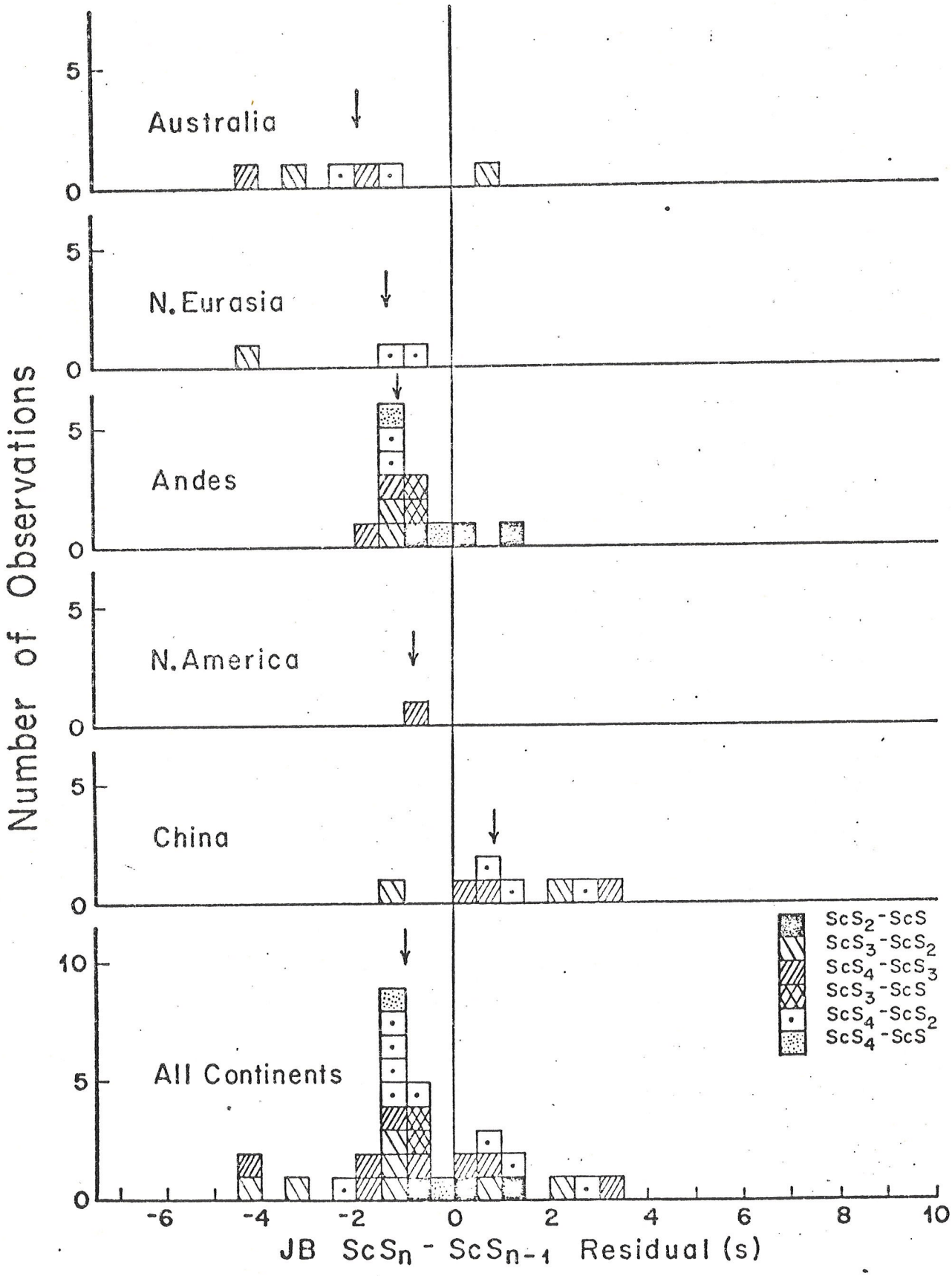
CONTINENTS
Australia
N. Eurasia
Andes
N. America
China
All Continents
Number of Observations
JB ScSn - ScSn-1 Residual (s)
ScS2-ScS
ScS3-ScS2
ScS4-ScS3
ScS3-ScS
ScS4-ScS2
ScS4-ScS

Figure 3.

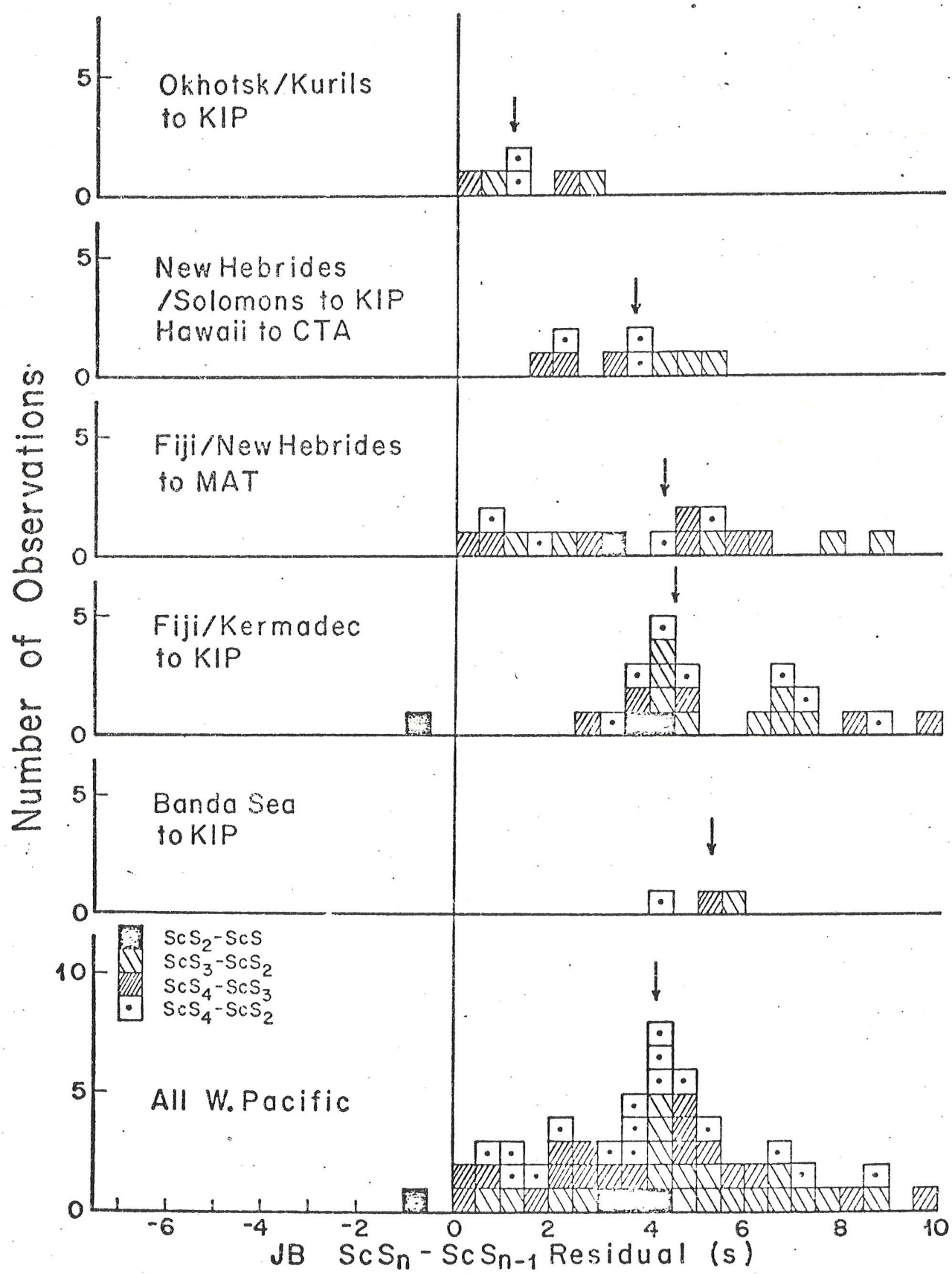
W. PACIFIC
Okhotsk/Kurils to KIP
New Hebrides /Solomons to KIP Hawaii to CTA
Fiji/New Hebrides to MAT
Fiji/Kermadec to KIP
Banda Sea to KIP
All W. Pacific
ScS2-ScS
ScS3-ScS2
ScS4-ScS3
ScS4-ScS2
Number of Observations
JB ScSn - ScSn-1 Residual (s)

Figure 4.

Determination of the Earth's density

We have seen how body wave seismology can be used to determine $\alpha(r)$ and $\beta(r)$ but data $T(\Delta)$ and/or $p(\Delta)$ or $\tau(p)$ provide no constraints at all on density $\rho(r)$, gm cm^{-3}.

Reflection coefficients at an interface do depend on all 3 of (ρ_1, ρ_2), (κ_1, κ_2) and (μ_1, μ_2)

medium 1

---

medium 2

In principle measurements of, say, PcP/P amplitude ratios can yield information about $\Delta\rho$ at CM bdry. People have tried this with mediocre success. In gen'l body wave amplitudes are not very reliable data, in contrast to travel times which can be measured very accurately.

Historical approaches to $\rho(r)$ determination

1. pre-seismology: only data geodetic. We have seen how $\bar{\rho}$ and C/Ma^2 measured: $\bar{\rho} = 5.517$ gm cm^{-3}, $C/Ma_e^2 = 0.33089$. Only 2 constraints. Early models were 2 parameter models, e.g. Thomson + Tait (1879): two layer model, mantle + core, find ρ_m and ρ_c (note: they didn't even know core radius). Wiechert (1897) took $\rho_m = 3.2$ (heavy surface rocks) and solved for core radius.
∃ other 2 parameter possibilities, e.g. Roche model (1848)
$$\rho(r) = \rho_0 (1 - Kr^2),$$ quadratic

2. The Adams-Williamson relation (1923)

This famous relation enables us to determine $\rho(r)$ from $\alpha(r)$ and $\beta(r)$ subject to certain assumptions about the makeup of the mantle. These are:

1. the material comprising the mantle (or any other region under study) is <u>chemically homogeneous</u>, e.g. Fe/Mg ratio does not change with depth.

historically this method was used to infer $\rho(r)$ in <u>mantle</u>.

* 2. the temperature distribution as a function of depth is <u>adiabatic</u> (we'll talk about what this means)

3. no major <u>phase changes</u> occur

* The last 2 may be summarized in the single statement that $dS(r)/dr = 0$ where $S(r)$ is the <u>entropy</u> of the mantle.

<u>Intuitively</u> we know that:

1. incompressibility depends on $\rho(r)$ and velocities $\alpha(r)$, $\beta(r)$
2. $\rho(r)$ depends on incompressibility and hydrostatic pressure
3. hydrostatic pressure depends on $\rho(r)$

The AW relation puts these interdependences into

one equation.

Recall the first of the above 3:

$$\alpha = \sqrt{\frac{K + \frac{4}{3}\mu}{\rho}} \quad , \quad \beta = \sqrt{\frac{\mu}{\rho}}$$

Define a new variable $\phi(r)$

$$\boxed{\phi \equiv \frac{K}{\rho} = \alpha^2 - \frac{4}{3}\beta^2}$$

Thus $K(r)/\rho(r)$ is known if $\alpha(r)$ and $\beta(r)$ are. This is relation 1.

Recall defn of K = incompressibility:

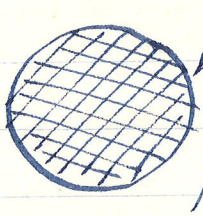

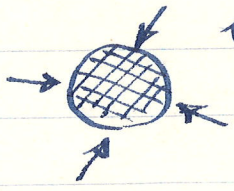

$$K = -\frac{dp}{(dV/V)}$$

- so $K > 0$ since dV will be negative for $dP > 0$

fractional change in volume

Now $\frac{dV}{V} = -\frac{d\rho}{\rho}$, fractional change in density (if volume decreases density goes up)

Thus $\kappa = \frac{dp}{(d\rho/\rho)}$ or

$$\boxed{\frac{\kappa}{\rho} = \phi = \frac{dp}{d\rho}}$$

But wait a minute. Clearly dV or $d\rho$ of a material does not depend only on dp, also depends on whether or not we heat it, i.e. on dT (thermal expansion / contraction).

Two extreme possibilities:

1. isothermal compression: T remains constant
2. isentropic or adiabatic compression: no heat allowed to flow in or out of sample; sample ∴ heats up when compressed.
   example: air in bicycle pump

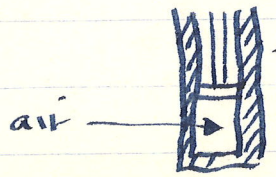

Which do we want? The question is: which corresponds to the passage of a seismic wave?

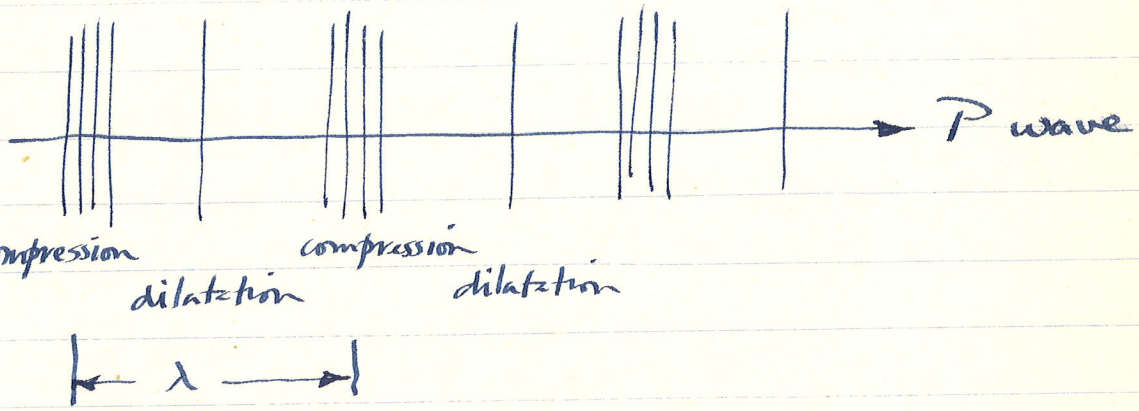

For wave propagation to be isothermal heat would have to flow from region of compression to region of dilatation as fast as the wave propagates. As we've seen heat diffusion in ordinary materials $\kappa \sim 0.01$ cm^2/s is a much, much slower process.

Hence wave propagation is adiabatic

$$\alpha = \sqrt{\frac{K_{adiabatic} + \mu}{\rho}}$$

, the $\kappa(r)$ measured by seismology is $K_{adiabatic}$.

A famous historical mistake: Newton in the Principia assumed sound waves in

air were isothermal, got wrong answer for speed of sound by $\sqrt{\gamma} \sim \sqrt{1.4}$, tried to explain it away by effects of humidity, etc., his "justification" makes interesting reading, corrected ~ 100 yrs. later by Laplace.

Thus $\kappa = \rho (dp/d\rho)_S$

$$\phi = \frac{\kappa}{\rho} = \left(\frac{dp}{d\rho}\right)_S$$

constant entropy (this the state function that is constant in an adiabatic process)

Now how does $\rho(r)$ depend on $\kappa(r)$ and $p(r)$, i.e. relation 2?
In thermodynamic equilibrium

depends on what it's made out of and on pressure and temp.

$\rho = \rho(p, T,$ chemical comp.)

or, alternatively, better for our purposes,

$$\boxed{\rho = \rho(p, S, \text{chemical comp.})}$$

Thus, differentiating

$$\frac{d\rho}{dr} = \left(\frac{\partial \rho}{\partial p}\right)_{S,Fe\ldots} \frac{dp}{dr} + \left(\frac{\partial \rho}{\partial S}\right)_{p,Fe\ldots} \frac{dS}{dr} + \left(\frac{\partial \rho}{\partial Fe}\right)_{p,S} \frac{dFe}{dr} + \ldots$$

$\frac{d\rho}{dr}$: radius in mantle

$\left(\frac{\partial \rho}{\partial p}\right)_{S,Fe\ldots}$: for same material at const. entropy

$\left(\frac{\partial \rho}{\partial S}\right)_{p,Fe\ldots}$: for same material at const. pressure

$+ \ldots$: other changes in chemistry.

↖ no phase changes + temp. adiabatic

We now assume that $dS/dr = 0$ and $dFe/dr \ldots = 0$ in mantle

↑ same chemical comp. throughout

In that case: $\frac{d\rho}{dr} = \left(\frac{\partial \rho}{\partial p}\right)_{S,Fe\ldots} \frac{dp}{dr}$

↖ this is just ϕ^{-1}!

$$\boxed{\frac{d\rho}{dr} = \phi^{-1} \frac{dp}{dr}}$$

Now for relation 3: the equation of hydrostatic balance which relates the pressure gradient dp/dr to $\rho(r)$.

The grav. acceleration downward at any radius r is given by

$$g(r) = \frac{G}{r^2}\left[4\pi \int_0^r \rho(r)\, r^2\, dr\right]$$

mass within sphere of radius r (the mass outside does not attract)

Draw spherical part of picture below first

Consider a 1 cm x 1 cm pillbox at radius r of thickness dr

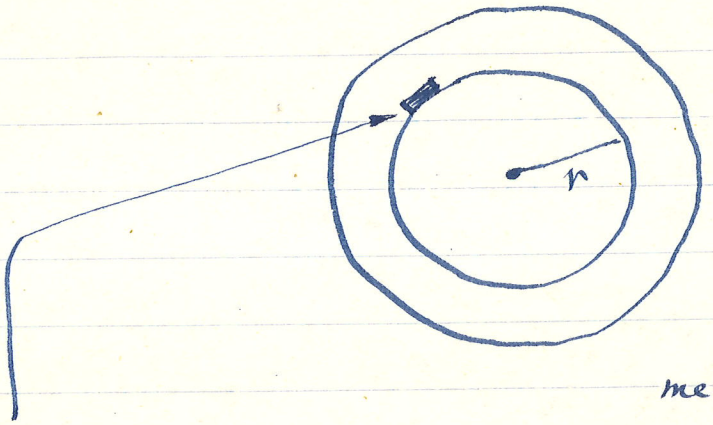

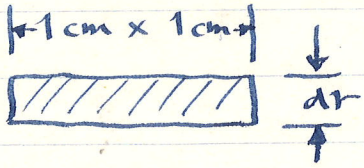

measured per unit area

Balance forces on this pillbox.

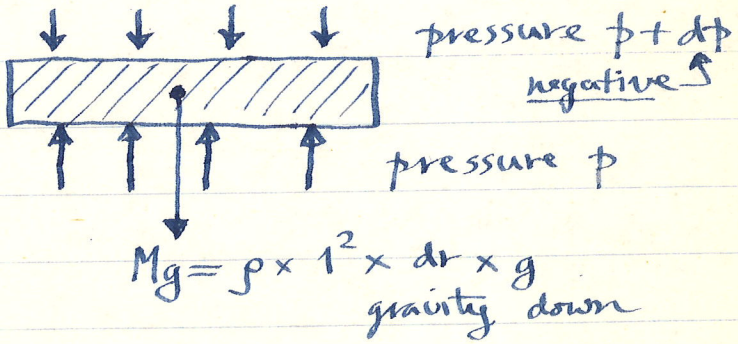

dp/dr is negative

up : p

down : $p + dp + \rho g\, dr$

$= p + (dp/dr)\, dr + \rho g\, dr$

Thus $$\boxed{dp(r)/dr = -\rho(r) g(r)}$$

↑ equation of hydrostatic balance

Thus finally putting everything together

$$d\rho/dr = \phi^{-1}\, d\phi/dr$$

$$\boxed{\frac{d\rho(r)}{dr} = -\frac{4\pi G \rho(r)}{r^2 \phi(r)} \int_0^r \rho(r)\, r^2\, dr}$$

↑ this is the AW relation (1923)
Given $\phi(r)$ an integro-differential eqn for $\rho(r)$.

Can also be written as 2 coupled ODE's.
Let

$$\boxed{m(r) \equiv \text{mass inside radius } r}$$

i.e. $$m(r) = 4\pi \int_0^r \rho(r)\, r^2\, dr$$

$$dm/dr = 4\pi \rho r^2$$

$$\boxed{\begin{aligned} dp/dr &= -Gm\rho/r^2\phi \\ dm/dr &= 4\pi r^2 \rho \end{aligned}} \quad *$$

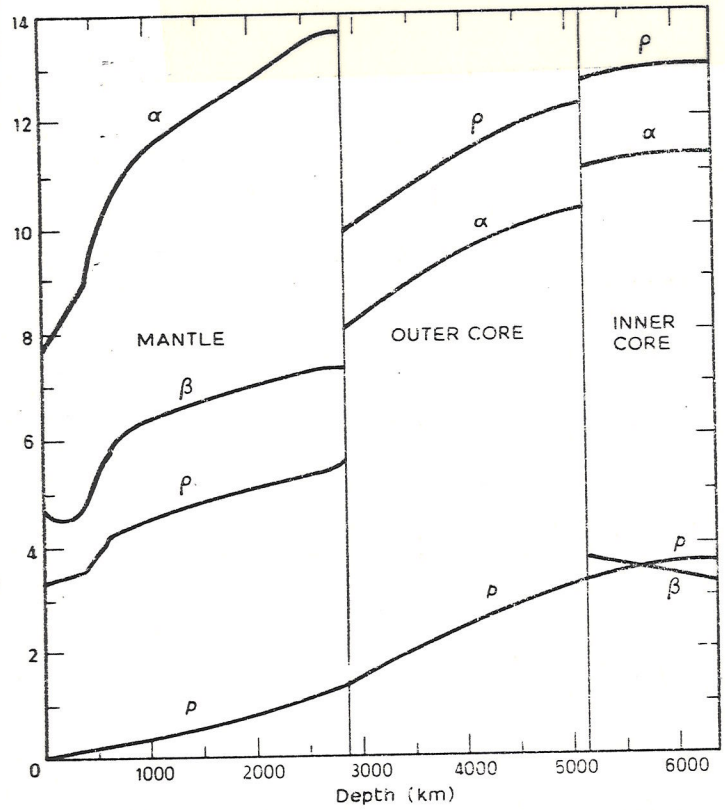

Fig. 16.1. Distributions in the Earth of the density ρ (g/cm^3), pressure p (10^{11} N/m^2), and P and S velocities α and β (km/s)

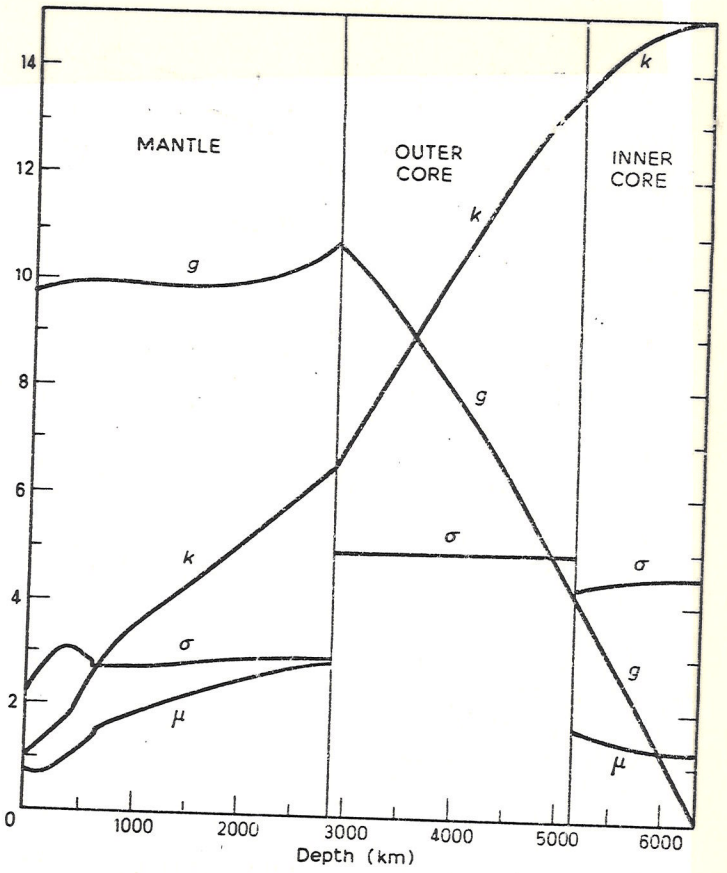

Fig. 16.2. Distributions in the Earth of the incompressibility k and rigidity μ (10^{11} N/m^2), gravitational intensity g (m/s^2), and Poisson's ratio σ. (The scale unit for σ corresponds to 0·1.)

If $\rho(r)$ known for some range of r and <u>starting values for $m(r)$ and $\rho(r)$ are selected</u> then $\rho(r)$ can be determined by <u>numerical integration</u>. Equations * give <u>slopes</u> of ρ and m in terms of ρ, m and ϕ. Can use to extrapolate to next radius increment up or down, then repeat for entire interval.

1936 this done by K. Bullen without aid of electronic calculator. He ~~assumed~~ integrated <u>down</u> from surface to CM bdry. Starting value for $m(r)$ then known. He assumed

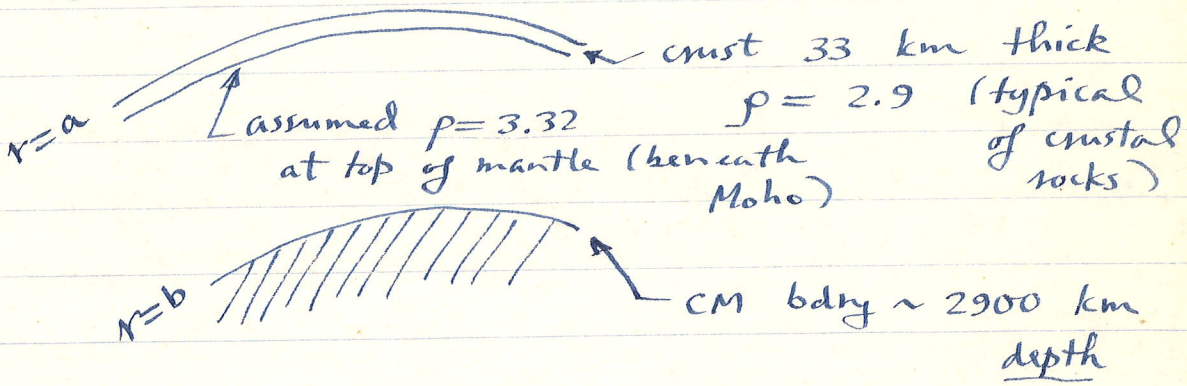

This yielded a <u>trial</u> $\rho(r)$ in mantle plus crust. He then computed

$$C_{\substack{\text{mantle} \\ +\text{crust}}} = \frac{8\pi}{3} \int_b^a \rho_{\text{trial}}(r)\, r^4\, dr$$

and subtracted from known $C_\oplus$ to get

a trial value for C_{core}, moment of inertia of core:

$$C_{\substack{core \\ trial}} = 0.57\, M_{core}\, b^2$$

(M_{core}: known (simply $M_\oplus - M_{\substack{mantle \\ + crust}}$))

This can be discounted since $0.57 > \frac{2}{5}$. would imply core denser on outside than inside (C of a mass shell is $\frac{2}{3} M b^2$ so would imply core almost hollow !). Contradiction.

Hence Bullen concluded one of the assumptions underlying procedure wrong:

1. starting value for $\rho = 3.32$ gm/cm^3
2. chemical comp. of mantle uniform
3. entropy $S(r) =$ const.

Further calculation showed that $\rho_{starting}$ would have to be increased to at least 3.7 gm cm^{-3} to reduce 0.57 to 0.40. This untenable on petrological grounds, $\rho_{starting} \approx 3.32$ typical of peridotitic rocks thought to be slices of mantle brought up to surface.

This first evidence (1936) that mantle either chemically zoned or ∃ phase changes. Typically the entropy of a material of constant composition suffers a jump ΔS in entropy when a change in phase occurs, in fact $\Delta S = \frac{1}{T}\Delta H$, ΔH = latent heat of transformation.

Now realized that major reason for Bullen's result is upper mantle phase changes, esp. near 400 and 650 km depth. We shall discuss mineralogy of these in more detail later.

400 km: olivine (major constituent of upper mantle) rearranges lattice to spinel structure, more closely packed.
650 km: increasing pressure causes further rearrangement, closer packing, Si-O coordination increases from 4 to 6. Perovskite structure.
AW relation can now be used in reverse. The density profile can now be inferred with no "extra" assumptions from inversion of free oscillation periods, since these in contrast to $T(\Delta)$ depend (among other things) on $\rho(r)$.

Normal mode models of $\rho(r)$ show steep increase in upper mantle due to phase changes, rearrangement of atomic lattices, there is however not enough resolution to distinguish between

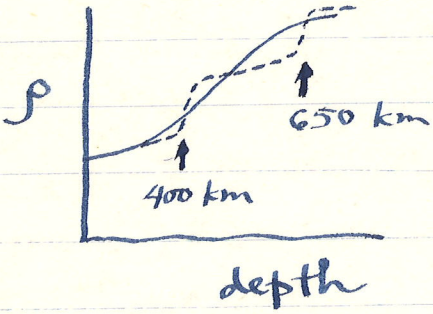

Increase in lower mantle is smooth to $\rho \approx 5.5$ gm/cm^3 above CM bdry where it jumps to $\rho \approx 10$ gm/cm^3, Fe-Ni core, again smooth increase to $\rho \approx 12$ gm/cm^3 above inner core boundary, increases there to $\rho \approx 13$ gm/cm^3.

$\Delta\rho$ at IC-OC boundary not well determined but of some importance. If $\Delta\rho$ is sufficiently large that IC must be of heavier material than fluid core (chemical fractionation upon freezing or solidification) then light residue left behind in fluid could cause chemical convection and thereby drive geodynamo. Suggested by Braginskii.

Our picture of ⊕'s structure is thus:

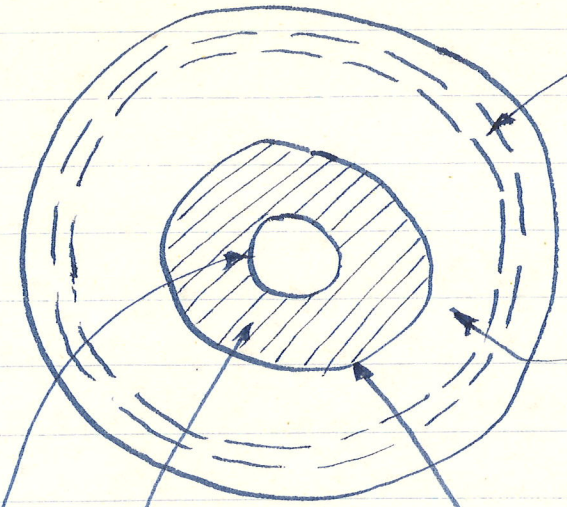

400 – 650 km depth called transition zone

upper mantle (down to ~ 650 km) phase transitions, e.g. olivine → spinel → Si perovskite

lower mantle (below 650) uniform comp. + phase increase in ρ smooth due to adiabatic compression

major comp. boundary silicate rock overlying Fe core

smooth increase in density due again to adiabatic compression

phase boundary (solidification of IC), whether ∃ comp. diff. as well is not certain, depends on magnitude of jump $\Delta\rho$, solidification will result in some increase $\Delta\rho$ (ice is one of very few materials which become less dense upon freezing)

If AW relation is integrated downward from 650 km depth to CM bdry can compare $\rho_{\text{normal modes}}$ with ρ_{AW}, can do same in core. This done for PEM by Dziewonski et al. (PEM has discont. at $r = 5700$ km or 671 km depth rather than 650).

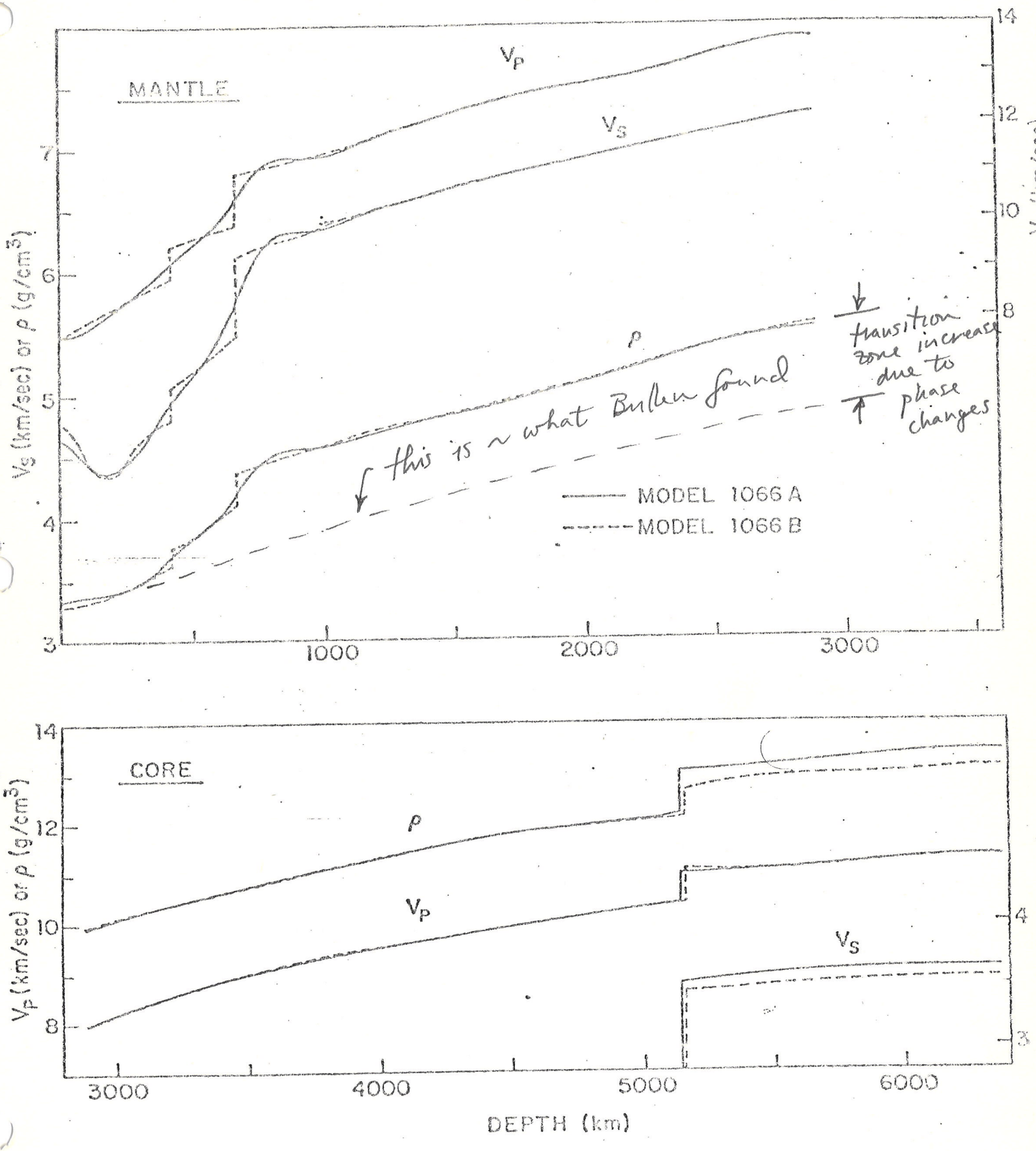
MANTLE
V_P
V_S
ρ
this is ~ what Bullen found
transition zone increase due to phase changes
MODEL 1066 A
MODEL 1066 B
V_S (km/sec) or ρ (g/cm^3)
V_P (km/sec)
3
4
5
6
7
8
10
12
14
1000
2000
3000
CORE
ρ
V_P
V_S
V_P (km/sec) or ρ (g/cm^3)
V_S (km/sec)
8
10
12
14
3
4
3000
4000
5000
6000
DEPTH (km)

Table 5.

Radius (km)	ρ (g/cm^3)	$\rho - \rho_{AW}$ (g/cm^3)
0	13.012	0.002
300	12.993	0.000
600	12.937	0.000
900	12.844	-0.001
1217	12.704	-0.001
1217	12.139	-0.015
1500	11.984	0.000
1800	11.789	0.006
2100	11.558	0.005
2400	11.288	0.000
2700	10.974	-0.006
3000	10.611	-0.007
3300	10.195	0.000
3486	9.909	0.017
3486	5.550	-0.008
3800	5.401	0.000
4100	5.253	0.002
4400	5.101	0.000
4700	4.943	-0.001
5000	4.779	-0.003
5300	4.611	0.000
5600	4.437	0.005
5700	4.377	0.009

Can be seen that $\rho - \rho_{AW}$ is negligibly small everywhere below 671 km depth, confirms above picture that dp/dr in lower mantle and in core [redacted] and in inner core is just due to adiabatic compression of chemically uniform materials.

Once $\rho(r)$ is known can find $g(r)$ from

$$\boxed{g(r) = \frac{4\pi G}{r^2} \int_0^r \rho(r)\, r^2\, dr}$$

and $p(r)$ from eqn of hydrostatic balance

$$dp(r)/dr = -\rho(r) g(r), \quad \text{or integrated form}$$

$$\boxed{p(r) = \int_r^a \rho(r) g(r)\, dr}$$

↑ this satisfies diff. eq. and b.c. that $p(a) = 0$

It is a curiosity that $g(r)$ is essentially constant (~ 9.8 cm/sec^2) throughout mantle, falls ~ linearly to zero at center of ⊕.

Recall: if $\rho(r) = \text{const}$, then $g(r) \sim r$,
in fact $g(r) = \frac{4}{3}\pi G \rho r$.

Pressure $p(r)$: 1 Pa = 1 N/m^2 = 10 dyne/cm^2

10^{11} Pa = 10^{12} dyne/cm^2

1 atm = 760 mm Hg = 10^6 bar or 1 Mbar
= 1.013 bars

pressure at center of $\oplus \approx$ 3.5 megabars
$\approx 3.5 \times 10^6$ atmospheres
$\approx$ 350 GPa

Given $\rho(r)$ can also find $\kappa(r)$ and $\mu(r)$ from

$$\mu = \rho\beta^2$$
$$\kappa = \rho\phi = \rho\left(\alpha^2 - \frac{4}{3}\beta^2\right)$$

These shown for Bullen's model HB1 in Fig. 16.2, this model a little older than 1066A, B and PEM, less resolution, but such plots are not very revealing anyway, what is more important is <u>comparisons</u> such as $\rho - \rho_{AW}$ and Δp at IC–OC bdry with that expected for constant composition.

3. Birch's "law": Francis Birch 1960's compiled laboratory measurements of v_p and ρ for a wide variety of rocks and minerals, oxides and silicates. P wave speed v_p or α measured ultrasonically. Noted the following empirical relation (not really a law)

$$v_p = A(\bar{M}) + B\rho$$

($\bar{M}$: mean atomic weight)

linear relation between P velocity and density, heavier materials are faster (this in spite of $\alpha = \sqrt{(K + \frac{4}{3}\mu)/\rho}$)

Slope B has value $B \approx 3 \frac{km/sec}{gm/cm^3}$

Recall M for common elements

O: 16.000

Si: 28.09

Fe: 55.85

Mg: 24.32

more Mg than Fe

$\bar{M}$ for typical mantle silicates $\approx$ 20-22

$(Mg, Fe)_2 SiO_4$

Data on oxides and silicates shown in Fig. 9-6. Velocity measured at 10 kbars (corresponds to ~ 30 km depth) to close cracks in rocks. Dashed lines for $\bar{M} = 19, 20$, etc.

Birch's "law" was thought until a few years ago to prevail through a phase transition (since it was seen to be applicable to such a wide range of minerals with different structures).

1961 (before development of normal mode inversion) Birch employed Birch's "law" to infer a density structure for mantle. He assumed that $\bar{M}$ was independent of depth (constant chemical composition).

After normal mode inversion had produced an assumption-free $\rho(r)$ Press and others sought to turn argument around, use Birch's "law" to find $\bar{M}(r)$ in the mantle, controlled principally by Mg/Fe ratio because $M_{Fe} > 2 M_{Mg}$).

Press employed an unsophisticated inversion

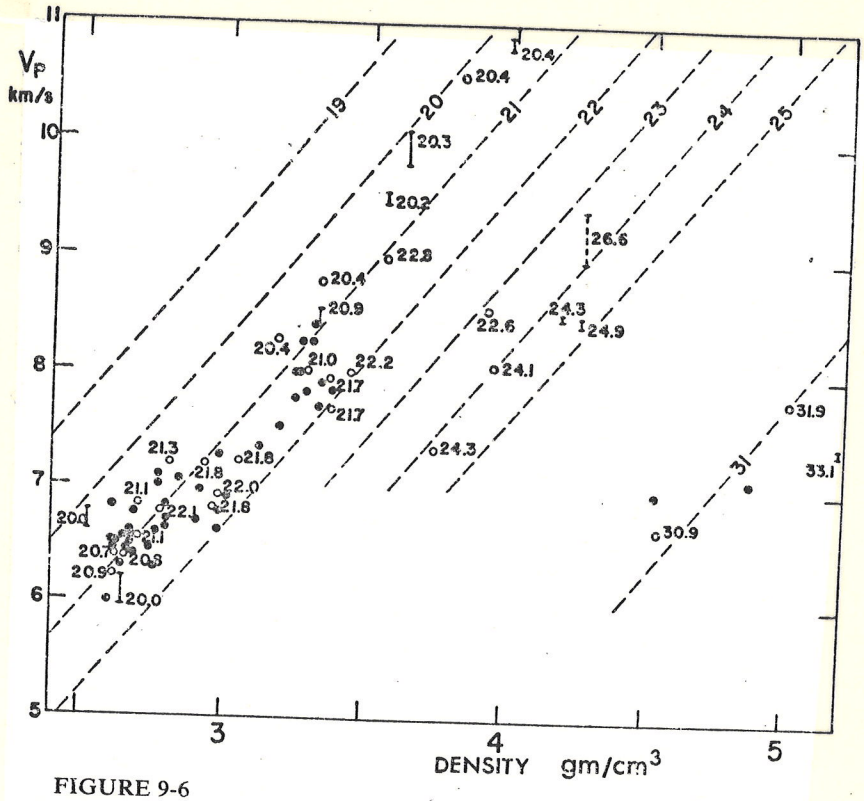

FIGURE 9-6
Velocity at 10 kbars versus density for silicates and oxides. The numbers attached to open circles are mean atomic weights. Dashed lines suggest variation for constant mean atomic weights. (*From Birch, 1961a, with permission. Copyright American Geophysical Union.*)

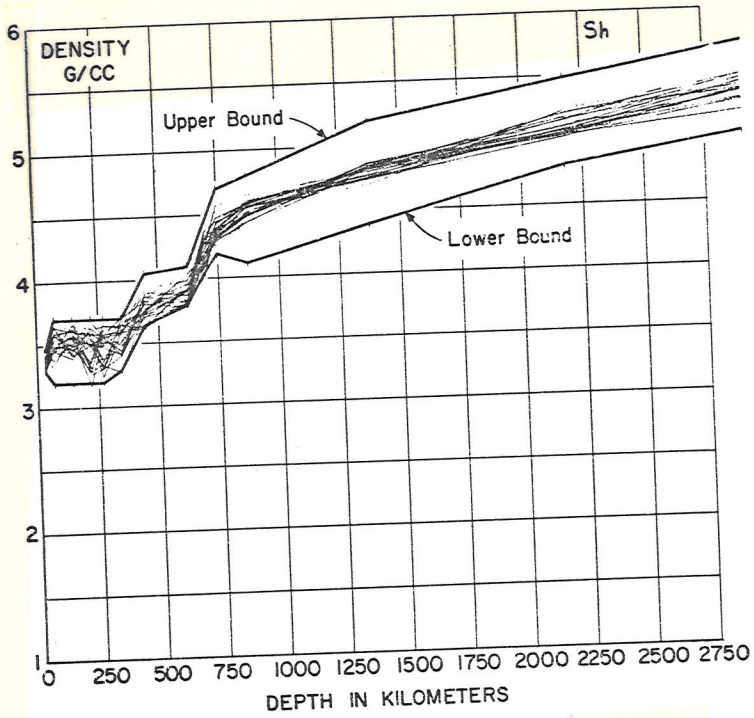

Fig. 9. Density models for the mantle using continental shield data.

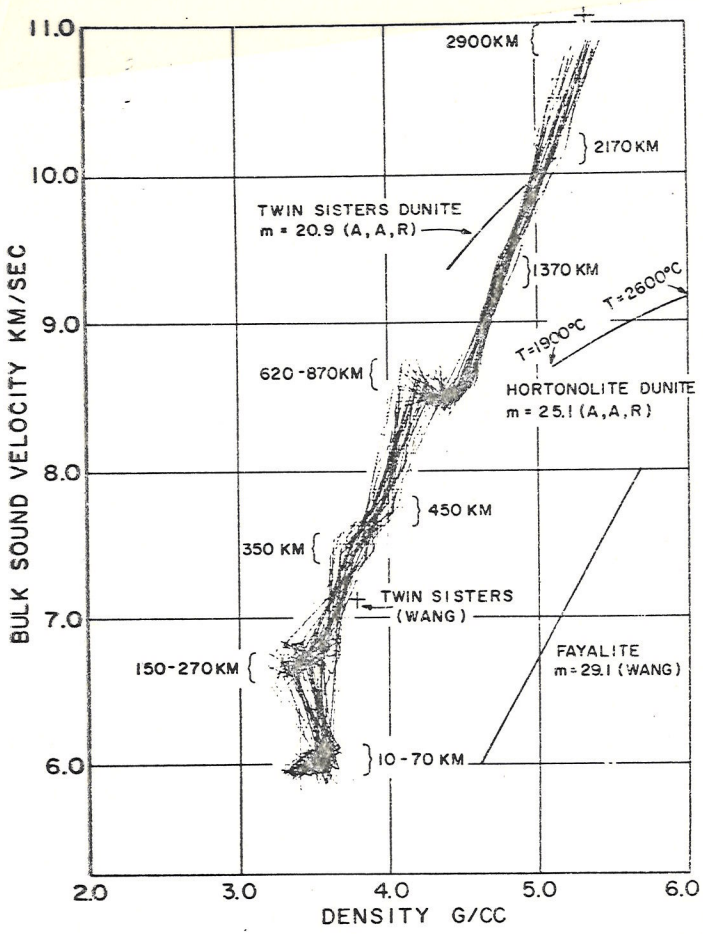

Fig. 24. Plot of bulk sound velocity against density derived from successful solutions. Comparison with shock wave derived curves for ultrabasic rocks according to Ahrens, Anderson, and Ringwood (1969) and Wang (1968). Wang's results for Twin Sisters dunite is a straight line connecting the two crosses. Ahrens', Anderson's, and Ringwood's results are indicated by *A*, *A*, *R*.

method, Monte Carlo inversion, generate models at random (within certain limits), cull out those which fit normal mode + travel time data. An example of successful density models shown in his Fig. 9.

His ρ models plotted against v_p in his Fig. 24

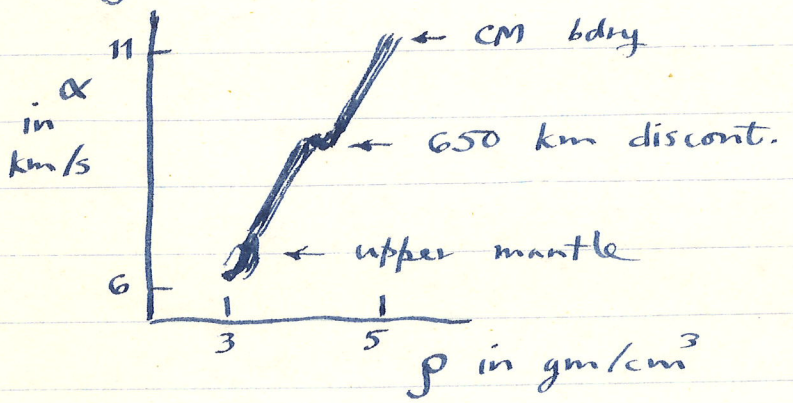

Has form of Birch's "law"

$$v_p = A + B\rho$$

But $A_{\substack{\text{above}\\650}} > A_{\substack{\text{below}\\650}}$.

Press concluded from this that:

$$\left.\begin{aligned} \bar{M}_{\substack{\text{above}\\650}} &\approx 20-21 \\ \bar{M}_{\substack{\text{below}\\650}} &\approx 21-22 \end{aligned}\right\} \text{a jump of about 1 unit in } M$$

↓ division at 650 km.

This would → chemical zonation of mantle: lower mantle richer in Fe, if upper and lower mantle not mixed, presumably

presumably they must convect separately.

Then 1974 Liebermann + Ringwood found that Birch's "law" does not apply thru a phase transition. They made static pressure experiments on olivine, germanate analogues, etc. We'll discuss these in more detail later.

They found that in the case of phase transitions which increase cation – oxygen coordination from fourfold to sixfold (this thought to characterize 650 km discont) that v_p vs. ρ trajectory tends to be offset by an amount "similar to the offset caused by an increase in $\bar{M}$ by about 1 unit".

The observed offset in Press' Fig. 24 thus need not ⇒ an increase in $\bar{M}$ at that depth. This now the favored interpretation.

They found $\Delta\alpha/\Delta\rho$ through a phase transition to be less than Birch's law:

$$\left(\Delta\alpha/\Delta\rho\right)_{\text{phase change}} \sim 1.9 \text{ (instead of 3)}$$

Table 9-4 CHANGES IN P VELOCITY AND DENSITY ACROSS SOME PHASE TRANSFORMATIONS. (*After Liebermann and Ringwood, 1973, and Liebermann, 1974*)

Phase transformation	$\Delta V_p/\Delta\rho$ [(km/sec)/(g/cm^3)]
Quartz-coesite (SiO_2)	5.7
Quartz-rutile (SiO_2)	3.0
Coesite-rutile (SiO_2)	2.5
Quartz-rutile (GeO_2)	2.2
Olivine-spinel (Mg_2GeO_4)	3.5
Olivine-spinel (Fe_2SiO_4)	2.5
Olivine-spinel (Ni_2SiO_4)	2.2
Olivine-beta (Mn_2GeO_4)	3.2
Pyroxene-ilmenite ($MgGeO_3$)	1.6
Pyroxene-ilmenite ($MnGeO_3$)	1.0
"Pyroxene"-garnet ($CaGeO_3$)	1.5
"Pyroxene"-garnet ($CdGeO_3$)	1.2
Ilmenite-perovskite ($CdTiO_3$)	2.0
Felspar-hollandite ($NaAlGe_3O_8$)	1.3

of $\Delta V_p/\Delta\rho$ (average $B = 1.9$) are generally smaller than given by Birch's rule applied to compounds of similar mean atomic weight ($B = 3.1$). They are also smaller than the B values applying during compression or thermal expansion of homogeneous material. Similar behaviour has been noted by Davies (1974) in the case of transformations into isochemical mixed oxides; moreover, it extends to the relationship between bulk sound velocity and density.[1,2]

These results indicate that the velocity-density trajectories followed during the compression of homogeneous materials are likely to be offset if these materials transform to phase assemblages characterized by higher cation-oxygen coordinations. In general, these offsets will be similar to the offset caused by an increase of mean atomic weight amounting to about one unit in $\bar{M}$. It follows that inferred offsets of this magnitude in the bulk sound velocity-density relationship in the mantle at a depth of about 650 km,[3] where it is believed that phase changes involving an increase of silicon coordination from fourfold to sixfold occur,[4] do not necessarily constitute evidence favouring an increase in $\bar{M}$ at this depth. This topic is taken up again in Chap. 14.

[1]Liebermann (1974).
[2]Davies (1974).
[3]E.g., Press (1970).
[4]Chapter 14.

MANTLE GEOPHYSICS

Mineralogical phase change at the 670-km discontinuity

Bernard J. Wood

THE boundary between the upper and lower portions of the Earth's mantle is generally taken to correspond to the worldwide seismic discontinuity at 670 km depth, at which the seismic-wave velocity increases by a few per cent[1] and the density of the silicate minerals increases. The simplest explanation, that the discontinuity is due to an isochemical phase transformation in a mantle of uniform composition, is disputed in the light of incompatible experimental data[2] on the thermodynamic and elastic properties of high pressure phases. An alternative model is that the mantle is chemically stratified with at least one major compositional discontinuity at 670 km and possibly other distinct layers at shallower depths[3]. But in a new experimental study[4], Ito and Takahashi show that an isochemical transformation in $(Mg,Fe)_2SiO_4$, the dominant component of the upper mantle, has many of the properties required to explain the 670-km discontinuity. Their results would thus be consistent with both upper and lower parts of the mantle being peridotitic in composition.

The question of whether the mantle, which is convecting vigorously, is chemically layered is crucial to understanding its dynamics and its chemical and physical history. Numerical simulations[5] indicate that even small compositional differences, equivalent to a 3-per-cent change in density, would be sufficient to inhibit convective exchange between the upper and lower mantle and hence to isolate the lower mantle from most plate-tectonic processes. Many geochemists have argued that such isolation occurs, on the grounds that it explains the apparent depletion of the source region of oceanic basalts in lithophile elements such as K, Rb, Cs, U and Th relative to the inferred composition of the bulk Earth. Modelling[6] of the isotopic evolution of this source region implies that it corresponds to about 30 per cent of the volume of the mantle, which happens to equal the volume of the mantle above 670 km.

Seismologically, the 670-km discontinuity is extremely sharp, giving rise to underside primary-wave reflections that require[7] the velocity increase to take place over a depth interval of less than 4 km. Isochemical transformations in complex systems are generally continuous and spread out, however, implying that they cannot, in general, give rise to reflections at the wavelengths of concern. Chemical stratification, on the other hand, would give a true discontinuity.

The experiments of Ito and Takahashi[4] relate to the conditions under which $(Mg,Fe)_2SiO_4$ in the spinel structure transforms isochemically to $(Mg,Fe)SiO_3$ perovskite plus $(Mg,Fe)O$ magnesiowustite at high pressures. The authors show that the transformation is extremely sharp for compositions with upper-mantle ratios of $Fe^{2+}/(Fe^{2+}+Mg)$ of about 0.1 and that it takes place under pressure conditions — 23 gigapascal (GPa) at 1,600 °C — that closely approximate those present at the 670-km discontinuity. For these low iron contents, the experimental data indicate that there exists a narrow transition interval of coexistence of high- and low-pressure phases and that the transformation pressure may either increase slightly or decrease as Fe is substituted for Mg (see figure). But even if we assume large uncertainties in the partitioning of Fe and Mg between low- and high-pressure phases, it is virtually impossible to generate an interval wider than 0.2 GPa (6-km depth interval) and values less than 0.05 GPa (1.5 km) are most likely. This leads to the unexpected conclusion that the isochemical transformation of $(Mg,Fe)_2SiO_4$ spinel to perovskite plus oxide is essentially discontinuous and is thus capable of acting as a seismic-wave reflector.

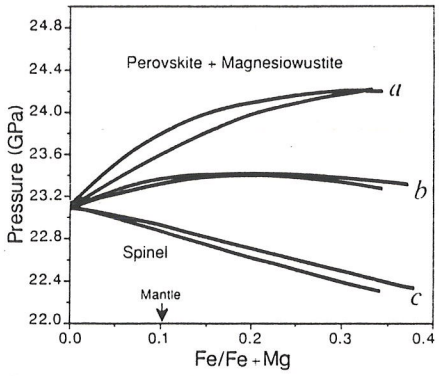

The breakdown of $(Mg,Fe)_2SiO_4$ spinel to perovskite and magnesiowustite at 1,600 °C (after ref. 4). Note that the transition interval of coexistence of all three phases has a maximum width of 0.2 GPa (6 km) if we use possible geometry *a*. The most likely geometries, however, are *b* or *c* which give extremely narrow transition intervals for upper-mantle values of $Fe^{2+}/(Fe^{2+}+Mg)$.

The phase transformation may exhibit one of the main features of the 670-km discontinuity, but is it consistent with other geophysical and geochemical data? Jeanloz and Knittle argue in another new paper[8] that the density of the lower mantle (known to an accuracy of about 0.5 per cent) is too high for it to be compositionally equivalent to upper mantle peridotite. From their measurements of the compressibility and thermal expansion of the perovskite phase, they infer that the lower mantle is enriched in iron relative to the upper mantle and hence, by implication, that the 670-km discontinuity corresponds to both a chemical boundary and a phase transformation. This argument depends, however, on measurements of the thermal expansion of perovskite at low pressure, well outside the perovskite stability field[2], that gave a high coefficient of thermal expansion. There is doubt about the applicability of these data, collected on a metastable phase and requiring much extrapolation in pressure and temperature, because measurements of other perovskite-like phases[9] yield lower thermal expansions. Adoption of a smaller thermal expansion coefficient brings the density of lower mantle into approximate agreement with that expected for peridotite compositions (C.R. Bina and P.G. Silver, personal communciation).

Although geochemical data clearly show long-term segregation of the mantle into regions distinct in isotope and trace-element evolution, there is no requirement that these reservoirs exhibit gross differences in major-element composition or that they be radially distributed above and below 670 km depth. Furthermore, there is increasing seismological evidence that, at plate boundaries, subducting slabs penetrate into the lower mantle[10], implying that there must be at least limited chemical interchange across the 670-km discontinuity. Although chemical stratification at 670 km provides a convenient explanation for the isotope data, mixing of the upper and lower mantle would also be inhibited, but not completely stopped, by a phase transition with a slightly negative pressure–temperature dependence. The transformation studied by Ito and Takahashi fulfils this requirement. Thus the new experimental data indicate that a simple phase change explains the discontinuity. Measurements of the density of perovskite plus magnesiowustite under actual lower-mantle conditions are required to refute or confirm this. □

Bernard J. Wood is in the Department of Geology, University of Bristol, Bristol BS8 1RJ, UK.

1. Dziewonski, A.M. & Anderson, D.L. *Phys. Earth planet. Inter.* **25**, 297–356 (1981).
2. Knittle, E., Jeanloz, R. & Smith, G.L. *Nature* **319**, 214–216 (1986).
3. Anderson, D.L. & Bass, J.D. *Nature* **320**, 321–328 (1986).
4. Ito, E. & Takahashi, E. *J. geophys. Res.* **94**, 10637–10646 (1989).
5. Christensen, U.R. & Yuen, D.A. *J. geophys. Res.* **89**, 4389–4402 (1984).
6. Wasserburg, G.J., & De Paolo, D.J. *Proc. natn. Acad. Sci. U.S.A.* **76**, 3594–3598 (1979).
7. Lees, A.C., Bukowinski, M.T. & Jeanloz, R., *J. geophys. Res.* **88**, 8145–8159 (1983).
8. Jeanloz, R. & Knittle, E. *Phil. Trans. R. Soc.* A**328**, 377–389 (1989).
9. Hill, R.J. & Jackson, I. *EOS* **70**, 475 (1989).
10. Creager, K.C. & Jordon, T.H. *J. geophys. Res.* **91**, 3573–3589 (1986).